



# Effect of Pulsed TIG Welding Parameters on the Microstructural Evolution and Mechanical Properties of Dissimilar AA6061-T6 and AA7075-T6 Weldments

Md Saquib Bin Reyaz<sup>1</sup> · Amar Nath Sinha<sup>1</sup> · Husain Mehdi<sup>2,3</sup> · Qasim Murtaza<sup>3</sup>

Received: 23 September 2023 / Accepted: 22 November 2023 / Published online: 18 December 2023  
© King Fahd University of Petroleum & Minerals 2023

## Abstract

AA6061-T6 and AA7075-T6 aluminium metals are broadly used in structural and aerospace sectors due to their exceptional features, but fusion welding causes thermal cracks, high residual stresses, and coarse grains, weakening joints. To solve these issues, pulsed tungsten inert gas (P-TIG) welding was used to improve the grain structure and mechanical features of the dissimilar joints. In this investigation, four peak currents (110, 120, 165, and 175 A) and four pulse frequencies (4, 8, 12, and 16 Hz) with constant base current, pulse on time, and argon flow rate were utilized, and the microstructural features were investigated and correlated with the joint's mechanical properties. The welded sample P4 developed a void-free joint with the maximum tensile strength (~ 201 MPa), elongation (~ 17%), microhardness (~ 101 HV), and compressive residual stresses (~ 76 MPa) compared to other welded samples. Microstructural evolutions revealed that, as the pulse current and frequencies increased, the grain refinement and grain boundary transformations across the FZ became more pronounced, and the segregation of alloying elements was lower. Specifically, for welded samples P4, the average grain size decreased to 21  $\mu\text{m}$ , and the grain boundary transformations reached 73.32%. Moreover, the orientation density value of the welded joints was much lower than that of the base metals, suggesting that the texture was greatly reduced after welding, which further reduced the anisotropy of the mechanical properties.

**Keywords** P-TIG · Aluminium alloys · Electron backscattered diffraction · Tensile strength · Microhardness · Residual stress

## 1 Introduction

The use of dissimilar metal joints is on the rise in industries including the automotive, electronics, and energy sectors. Heat-treated aluminium alloy AA6061-T6 is commonly used for bridge girders, military trucks, road storage containers, and rail transport systems due to its superb weldability, superior corrosion resistance, and high strength properties. Mg and Si are the primary alloying elements of 6061-T6 aluminium alloy, and they contribute to its strength via precipitation hardening [1, 2]. Cast Al-Zn-Mg alloy

AA7075-T6 is broadly utilized in the vehicle and aviation sectors due to its high strength, low quenching sensibility, broad range of usable solution heat treatment conditions, and rapid natural ageing capabilities [3]. Hot cracking is a common problem in almost all aluminium alloys that may be heat treated. Hot cracking in the weld and coarse columnar grains, caused by the dominant temperature conditions during weld metal solidification, is the primary issues with the fusion welding of these alloys [4]. Welds may have significantly diminished mechanical characteristics if they include coarse grains and fractures [5, 6]. Due to the elevated temperatures and heat gradients in welded joints compared to cast metal, as well as the epitaxial character of the growth process, it is especially important to control the solidification structure in welded joints. Refining the grain structures in the fusion zone may help regulate solidification cracking. Solidification cracking is more common in coarse columnar grains than in fine equiaxed grains. It is possible that this is because grains with fine equiaxed are more capable of deforming to meet contraction strains [7]. So, numerous

✉ Md Saquib Bin Reyaz  
mdr.phd19.me@nitp.ac.in

<sup>1</sup> Department of Mechanical Engineering, National Institute of Technology Patna, Patna, Bihar 800005, India

<sup>2</sup> Department of Mechanical Engineering, Meerut Institute of Engineering and Technology, Meerut, India

<sup>3</sup> Department of Mechanical Engineering, Delhi Technological University, Delhi 110042, India



researchers have offered several strategies for improving the quality of refined grains [8–10], which rely on regulating the cooling of the molten metal puddle. Such approaches involve nucleation facilitated by an incubator [11, 12], interlayer cold working [13], weld arc oscillation, and alternative techniques for agitating the molten metal pool [14, 15], as well as pulse welding current [8–13]. All of these methods of external melt processing work on the same principle: They eliminate the need for a grain refiner in order to get around the restrictions placed on grain refining by the constitutional undercooling mechanism.

Pulsed tungsten inert gas (P-TIG) welding is a modified version of tungsten inert gas (TIG) welding. It was developed in the 1950s and involves cycling the welding current between high and low levels at a predetermined frequency [6, 16]. The peak current is frequently adjusted to achieve sufficient penetrability and profile of the bead, while the minimum current is usually set to maintain a stable arc. Similar to conventional constant current welding, this technique reduces heat loss through conduction into the neighbouring parent material and effectively utilizes arc energy to fuse a specific area within a short period. As a result, the weld is formed by a sequence of overlapping fragments. Because the base material is heated briefly during peak current pulses, the thermally affected zone is smaller compared to continuous current welding. This method not only improves the quality of the weld, but also guarantees the arc's stability [17, 18]. Pulsed current is also superior to other methods of grain refinement since it does not need the purchase of any extra equipment.

Extensive study has shown this approach to reduce distortion, residual stresses, and heat input while improving bead shape, heat sink variation tolerance, and heat input efficiency [16]. Pulsed current welding has several metallurgical advantages, including, but not limited to, improved grain size and substructure in the fusion zone, reduced HAZ width, and segregation control [6, 19]. These factors will aid in the improvement of mechanical characteristics. Several studies have employed current pulsing to improve the mechanical characteristics of welds and refine the grain structure of the fusion zones. Yuan et al. [6] investigated how the frequency of the pulsating current, used in plasma arc welding of the titanium plates, and affected the fineness of the grains formed after solidification. Dendrite fragmentation was shown to be the predominant mechanism for grain refinement in the joint, and the amount of grain refinement could be improved by increasing the pulsed current frequency. Kumar et al. [16] observed that manipulating the peak current and pulse frequency in the fusion area of TIG joints of AA6061 alloys had a notable effect on the refinement of grains. This refinement subsequently led to an increase in the tensile strength and percent elongation of the welds. Kumar and

Sundarrajan [20] studied the influence of pulse TIG welding parameters on the microstructure, notch tensile strength, and impact toughness of Al–Mg–Si alloy joints. Their findings revealed that the manipulation of peak current, base current, and pulse frequency led to the development of a refined equiaxed grain structure. A negative correlation has been established between the tensile strength of the notch and the impact toughness. Babu et al. [21] found that using current pulses resulted in a slight improvement in the quality of previous grains. This led to enhanced mechanical features such as microhardness, tensile strength, and ductility in TIG joints of Ti6Al4V in their original state. Yang et al. [22] discovered that the welding arc pressure produced by the pulse current could enhance grain nucleation and refine grains during high-intensity pulsed arc welding of Ti6Al4V. Yelamasetti and Rajyalakshmi [23] investigated the microstructural, mechanical, and residual stress behaviour of P-TIG welded joints of dissimilar AISI 316 and Monel 400 metals. They utilized non-pulse, pulse, and interpulse current during welding and observed an enhanced tensile and hardness properties with lower residual stresses for interpulse current followed by significant refinement of grains and lower thermally affected region. To investigate the metallurgical behaviour, Dev et al. [24] created distinct weld joints between Inconel and steel materials using P-TIG welding. They deduced that pulse current frequencies resulted in less segregation of alloying compositional elements and fine grain particles. In another study involving the P-TIG welding of dissimilar C-276 and Monel 400 materials, it was determined that there is less filler material fragmentation and a smaller partially molten zone, resulting in enhanced joint characteristics [25]. To examine the influence of pulse current on bead and thermal profiles, Reddy et al. [26] designed pulse TIG aluminium welding junctions. This welding process resulted in grain refinement and enhanced tensile strength characteristics. Balram et al. [27] welded same and distinct aluminium plates using TIG welding with both pulse and constant current modes. Both modes of welding were shown to generate compressive residual stresses at the centre of weld cross-section. However, the residual stresses created by the pulsed mode were smaller because there was less heat concentrated in the fusion region.

The aforementioned studies have shown that the peak current and pulse frequency of P-TIG parameters play a vital role in grain refinement and have proposed ideas for further investigation in this field. Pulsed tungsten inert gas welding is not often discussed for grain refinement in heat-treatable aluminium alloys, despite its effectiveness in producing improved weld microstructures on various metals. In addition, no systematic analysis of the effect of P-TIG parameters on the microstructure, mechanical, and residual stress characteristics of dissimilar AA6061-T6/AA7075-T6 aluminium joints has been performed.

To address this gap, the present study aimed to investigate the effect of P-TIG welding parameters, namely, peak current and pulse frequency on the microstructural evolution, mechanical features (such as tensile strength and microhardness), and residual stress of joints. The quality assessment of P-TIG joints involved the utilization of various analytical techniques, including optical microscopy, scanning electron microscopy (SEM), energy diffraction scanning (EDS), and X-ray diffraction (XRD). Using electron backscattered diffraction (EBSD), a comprehensive crystallographic texture investigation, including inverse pole figures, grain size distributions, misorientation angle distribution, and orientation distribution functions, has been conducted. Utilizing high-resolution X-ray diffraction (HRXRD), the residual stress distributions across the weld cross-section were investigated. In-depth tensile fractographic examinations were also conducted using SEM and spectroscopy. The study's results are thoroughly examined and analysed in relation to relevant scholarly articles in the subsequent sections.

## 2 Materials and Methods

In this investigation,  $150 \times 50 \times 6 \text{ mm}^3$  distinct AA6061-T6/AA7075-T6 plates were utilized as a base alloy and ER5356 [28, 29] as a filler wire with a diameter of 2.4 mm. Note that the T-6 temper in the aerospace industry corresponds to solution treatment for 1 h at 470 degrees Celsius, water quenching, and artificial ageing for 24 h at 120 degrees Celsius [30]. Table 1 shows the EDS-determined elemental compositions (in wt.%) of base alloys and filler wire metals. Experiments were conducted to determine the mechanical and residual stress characteristics of the base alloys, and the results are listed in Table 1.

Dissimilar butt joints were fabricated via an automated P-TIG welding power source (KEMPPI MasterTig 335 ACDC G) as shown in Fig. 1a. As shown in Fig. 1b, a 90-degree V-groove with a root spacing of 1.5 mm and a root face of 1.6 mm was configured for joining the two alloys (Table 2). Double pass welding was performed using a numeric control (NC) wire feed unit and robotic arm, as per the operating parameters mentioned in Table 3. Trial experiments and literature study determined welding process parameters and their ranges. Peak current, base current, pulse frequency, and pulse on time are frequently addressed for managing quality in P-TIG welding [16]. Peak currents below 110-A limit penetration and fusion. Peak current above 175 A causes weld bead undercut and spatter. Arc length is short if base current is less than 75 A, making filler metal installation problematic. The base current reaches 75 A as arc length grows, creating arc wandering. If pulse frequency was less than 4 Hz, beads resembled continuous current weld beads. Pulse frequency increases arc glare and splatter. Weld nugget formation is

less smooth when the pulse on time is less than 40% because the filler metal is not completely melted. At pulse times over 60%, filler metal and tungsten electrode melt too much. All welding runs employed A.C. polarity, 75-A base current, and 50% pulse on time. The torch angle was set as 90-degree, arc gap was 2.5 mm, pulse duration during peak stage was 1.8 ms, and pulse duration during base stage was 1.3 ms. The arc voltage was in the range of 14–17 V, and welding speed was 1.3 mm/s. Before welding, every plate underwent cleaning using acetone and a wire brush to eliminate oxide and other impurities. Clamp both plates firmly on a  $200 \text{ mm} \times 200 \text{ mm}$  mild steel base plate after cleaning. Plates were clamped and fastened to reduce welding warping. A 12-mm wide, 1.5-mm deep groove was carved in the backing plate's middle. Reduce joint origin cooling by cutting the groove to enhance penetration. The shield gas was 99.99% argon and the electrode 3.2-mm tungsten. Plates cooled to room temperature after welding. The amount of heat input generated during the pulse TIG welding was determined using Eq. (1) [31, 32].

$$Q_{\text{PTIG}} = \eta_{\text{arc}} \times \frac{V \times I_{\text{mean}}}{\text{WS}} \quad (1)$$

where  $Q_{\text{PTIG}}$  = heat input (J/mm),  $V$  = arc voltage (volt),  $\text{WS}$  = welding speed (mm/s),  $\eta_{\text{arc}}$  = arc efficiency = 60% [33], and  $I_{\text{mean}}$  = mean current determined by the following Eq. (2).

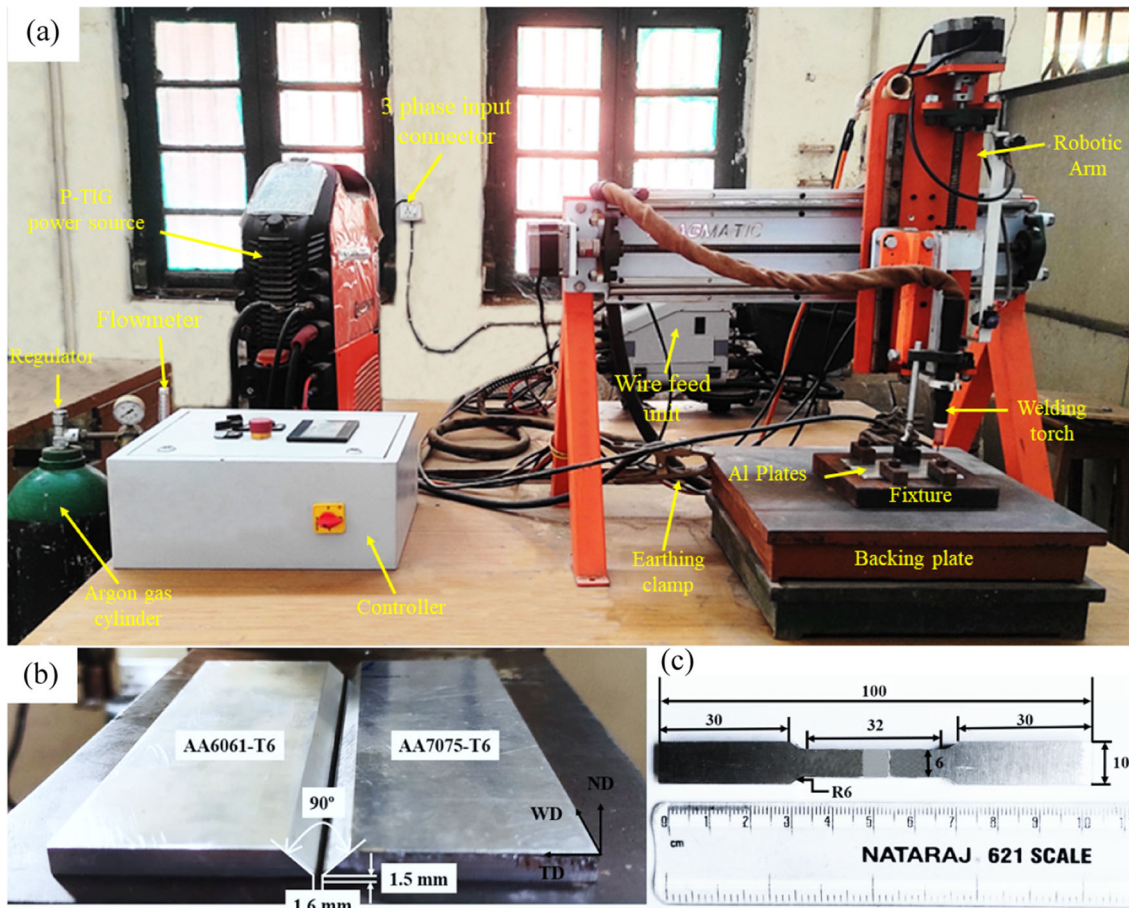
$$I_{\text{mean}} = \frac{I_p \times T_p + I_b \times T_b}{T_p + T_b} \quad (2)$$

$I_p$  and  $I_b$  are peak and base currents, while  $T_p$  and  $T_b$  are their corresponding pulse durations.

Wire electric discharge machining (WEDM) was employed to cut out the weld zone metallographic samples. The base alloys and welded samples were thoroughly ground and polished using 220–2200 grit abrasive sandpaper. Next, they were polished with 0.5- $\mu\text{m}$  diamond paste and etched with Keller's reagent for 15 s to create a mirror finish. However, to acquire proper metallographic results for the base metal AA6061-T6, the etched surface of this alloy was treated with a cotton swab dipped in a solution containing equal amounts of HF, HNO<sub>3</sub>, and methanol. Stereo microscope (Olympus-SC30, India) and SEM (Zeiss SUPRA40) with EDS setup were used to evaluate well-polished joints and element distribution. EBSD analysis required electropolishing the exposed surface of welded samples in an 80:20 methanol/perchloric acid solution at 15 V for 20 s at  $-5^\circ\text{C}$ . A SEM (Make: Quanta 3D FEG) was used to EBSD scan multiple welded samples' WMs. TSL OIM analysis software 8.0 was used to analyse scanned pictures with a step size of

**Table 1** Base metals and filler metal elemental composition (weight %) obtained by EDS analysis

Material	Cu	Zn	Mg	Mn	Cr	Ti	Fe	Si	Al
AA7075-T6	1.17	5.20	2.22	0.03	0.34	0.03	0.38	0.43	Balance
AA6061-T6	0.17	0.026	0.89	0.08	0.17	0.16	0.29	0.65	Balance
ER5356	0.014	0.05	4.9	0.16	0.10	0.07	0.15	0.04	Balance

**Fig. 1** a Experimental setup of an automated pulse TIG welding process, b V-groove details, and c tensile sample with proper dimensions**Table 2** Mechanical and residual stress properties of the base metals found experimentally

Metal	Average yield strength (MPa)	Average tensile strength (MPa)	Average percent elongation (%)	Average Vickers microhardness (HV)	Average residual stress (MPa)
AA7075-T6	410 ± 4.10	487 ± 7.22	12.6 ± 3.44	151 ± 1.68	- 33 ± 1.34
AA6061-T6	245 ± 2.38	288 ± 1.87	22.5 ± 5.14	110 ± 3.24	- 45 ± 2.17

0.2  $\mu\text{m}$ . Phase analysis using Empyrean, Malvern PANalytical diffractometer XRD. The  $\text{CuK}\alpha$  radiation was used to obtain XRD data with  $\lambda = 1.5418 \text{ \AA}$  and  $2\theta$  ranges of 10–90°.

Tensile, microhardness, and residual stress tests were conducted to examine the joint performance of dissimilar P-TIG welding. WEDM was utilized to cut transverse tensile samples in accordance with ASTM E8-M04, whose dimensional



**Table 3** Pulsed TIG welding process variables

Sample	Peak current (A)	Base current (A)	Pulse frequency (Hz)	Wire feed rate (m/min)	Heat input (kJ/mm)	Argon flow rate (l/min)
P1	110	75	4	1.2	0.61	20
P2	120		8	1.4	0.70	
P3	165		12	2.0	0.94	
P4	175		16	2.4	1.04	

**Table 4** Measuring parameters of the portable residual stress analyser

Apparatus	$\mu$ -X360n full 2D portable X-ray residual stress tester
XRT radiation	Cr-K $\alpha$
XRT voltage	20 kV
Measuring method	Single-incident angle method
Exposure time	30 s
Emission surface	Fe( $\alpha$ ) (211)
XRT amperage	1 mA
X-ray incident angle	45°
Collimator spot size diameter	$\phi$ 1 mm

characteristics are shown in Fig. 1c. Tensile tests were performed at room temperature on a Zwick/Roell Z250 model UTM with a capacity of 250 kN at a cross-head speed of 1 mm/min. Using a Vickers hardness analyser (UHL-002) calibrated to the ASTM E384-11 standard, microhardness tests were conducted from the centre of the weld cross-section to a highly polished surface. Throughout the testing procedure, a 100-gf load was administered for 15 s. The standard Cos $\alpha$  method was utilized to measure the residual stresses from the centre of the weld cross-section to the surface that had been mirror polished. More information about this method can be found in the works of the literature [34, 35]. Table 4 displays the measurable characteristics of the portable residual stress setup having an X-ray tube (XRT) as an essential component which incident the X-rays to the mirror finished surface of the joint.

### 3 Results and Discussion

#### 3.1 Weld Bead Appearance

Weld bead appearance is a crucial aspect of determining the success of welding, especially when working with dissimilar aluminium alloys. Figure 2 exhibits the optical images of weld bead surface (top and bottom side) of the welded samples at different process factors. A well-executed weld should

have a smooth and uniform appearance without any obvious defects such as cracks, porosity, or incomplete fusion. The automated welding process removes human error and keeps the arc gap constant, resulting in weld beads that are both crack-free and consistent when examined visually (Fig. 2a–d). The existence of uniform ripples with negligible spatter for all the joints ensures that the developed fixture serves the purpose. However, lack of fusion is observed in the bottom part of the bead near the joint line as marked by red area in Fig. 2a is due to incomplete mixing of base metals with filler metal. Whereas significant penetrations are observed on bottom view of the weld bead as shown from Fig. 2c and d, are due to increased weld thermal energy input. The shape and size of the weld bead had an impact on the mechanical properties of joints. ImageJ software indicates that the average values for weld width, penetration depth, and reinforcement lie within the approximate ranges of 10.1–13.8 mm, 3.1–6.5 mm, and 2.6–3.8 mm, correspondingly. An increased peak current and pulse frequency may result in increase in the width and depth of the welded seam. When the wire feed rate enhanced, the active area of the arc on the anode plate expanded, causing the anode spot to increase and the plasma flow speed at the arc centre to decrease. As a result, the radius of force distribution also became larger. Increasing the current causes, the plasma flow force distribution radius and peak pressure to rise, while keeping the arc length constant [36]. The arc force increases the penetration depth and breadth of the weld. These findings demonstrate that pulsing current frequency has a significant impact on the bead appearance of the weld, and these results are consistent with earlier findings [36, 37].

#### 3.2 Microstructural Evolution

Figure 3 shows the SEM microstructures of the base alloys AA6061-T6 and AA7075-T6, respectively. AA6061-T6 is characterized by coaxial grains, while AA7075-T6 displays elongated grains aligned in the rolling direction, as depicted in Fig. 3a and c. Black and white inclusion particles can be seen for both the base metals within the grains and at the grain boundaries, which are accountable for the intermetallic phase evolutions. XRD results exclusively displaying the

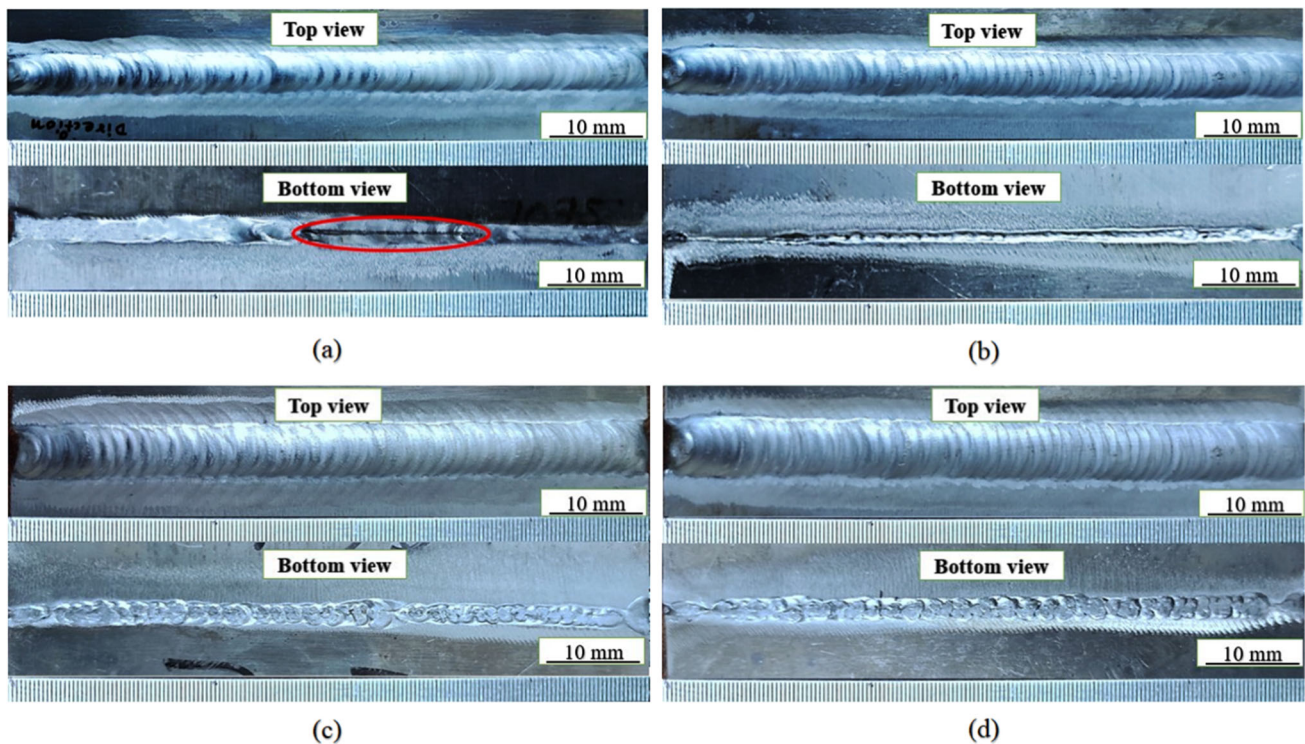


**Fig. 2** Optical images showing top and bottom side appearance of P-TIG welded samples **a** P1 (110 A, 4 Hz), **b** P2 (120 A, 8 Hz), **c** P3 (165 A, 12 Hz), and **d** P4 (175 A, 16 Hz)

presence of the  $Mg_2Si$  phase for AA6061-T6 and  $MgZn_2$  and  $Al_2CuMg$  isomorphous phases for AA7075-T6 alloy (Fig. 3b and d). It should be emphasized that  $Al_2Cu$  phase is not appeared in the XRD pattern for the base metal AA6061-T6, since the amount of this phase was too small [38]. The heat-treatable aluminium alloys gain strength by these intermetallics as a result of the precipitation hardening phenomenon [39].

When dissimilar metals are fusion welded with an external filler metal, a heterogeneous morphology of the joint is evolved due to the different solidification nature of the filler wire and dissimilar metals. Figure 4 illustrates the varying microstructural characteristics observed in various regions of the P-TIG welded sample P1 (110 A, 4 Hz). Figure 4a shows a macroscopic view of the welded cross-section, highlighting the various zones of the joint. Figure 4b–d shows the microstructures for the regions identified in Fig. 4a. The dendritic solidifying morphology with significant voids is observed on both the top and bottom sides of the fusion zone (FZ) (Fig. 4b and c). The region adjacent to FZ in the direction of the base alloy is the partially molten zone (PMZ), which is a solid–liquid interface zone close to the fusion line that contains a directional columnar structure along the direction of heat dispersion [40]. The PMZ of AA7075-T6 side clearly exhibits typically columnar grain structures with incipient melting at grain boundaries (see Fig. 4d) due to

the broad freezing temperature values of the base AA7075-T6 alloy [41]. However, the PMZ of AA6061-T6 side, the semi-molten surface of the grains is heated, non-spontaneous nuclei stick to the surface and grow towards the centre of the weld as columnar crystals, creating alternating crystallisation (see Fig. 4e) [36]. The area adjacent to PMZ towards the base alloy is the thermally affected zone (HAZ), whose grain structure is similar to corresponding base alloys and this experienced elevated temperatures (below the melting point) and formed a coarse grain affected by the weld thermal cycles [42]. The formation of voids in the welded samples P1 is due to the rapid cooling rate due to low heat inputs across the molten pool. For low heat inputs, the size of the weld molten pool is smaller, and the thermally affected area is smaller, resulting in a fast solidification of the weld pool and less time for hydrogen and oxygen gases to coalesce and escape. Thus, hydrogen was confined in the molten pool, leading to the formation of these voids in the FZ and compromising the weld joint's overall integrity. Moisture originated primarily from the atmosphere, the base alloys, the electrodes, and the filler wire [38].

The microstructure corresponding to the welded sample P4 (175 A, 16 Hz) is presented in Fig. 5. The intricate microstructures seen at the different regions indicated in Fig. 5a are depicted in Fig. 5b–e. At the FZ, the observed dendritic structure is significantly finer (Fig. 5b and c), and

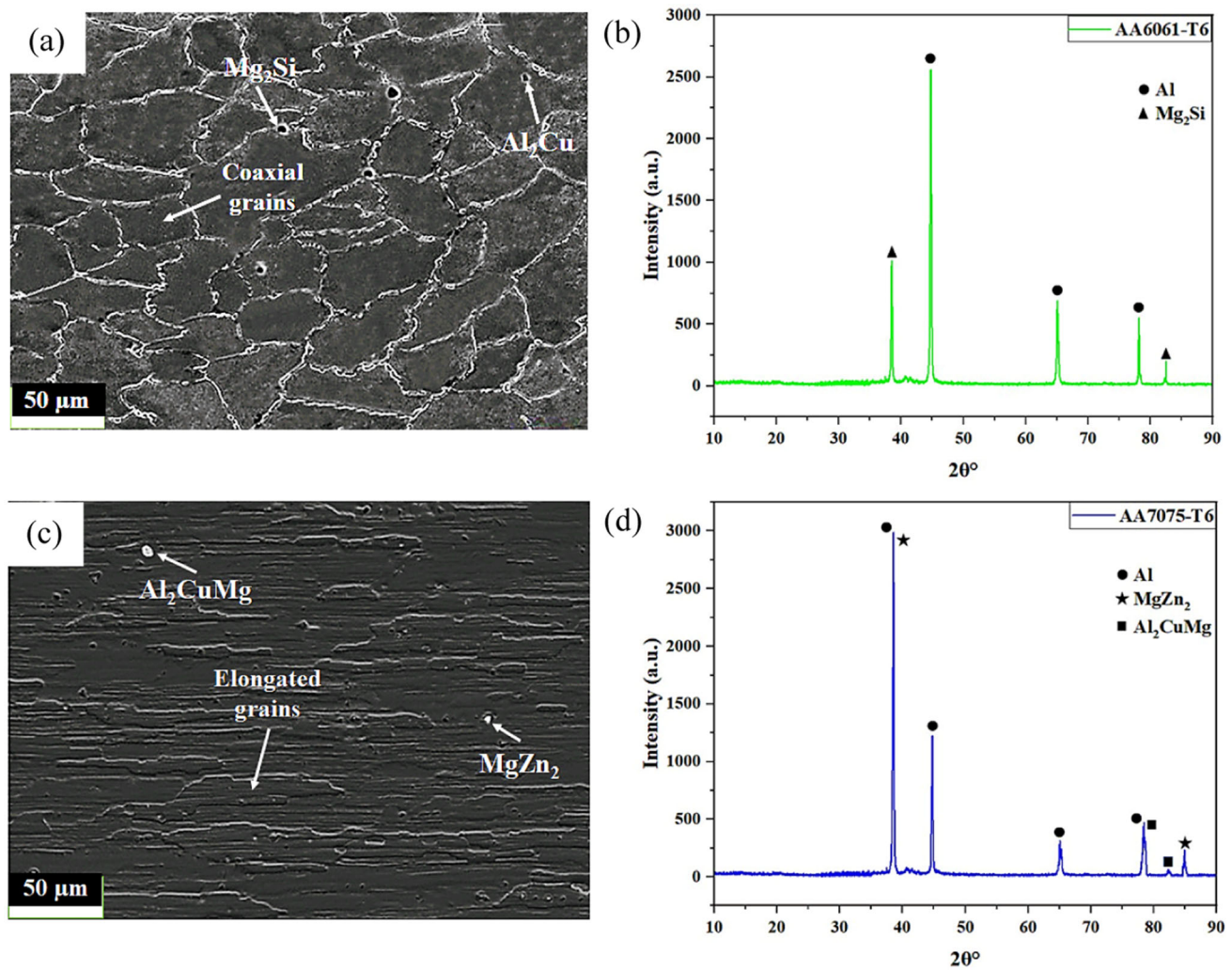


**Fig. 3** SEM micrographs and XRD peaks of the base metals: **a, b** AA6061-T6 and **c, d** AA7075-T6

the area of the PMZ is decreased significantly as compared to the welded sample P1 (see Fig. 5d and e). In addition, the area of the PMZ on both sides near the AA6061 side is lesser compared to AA7075 side. The increased thermal conductivity of AA6061-T6 results in a faster solidification [43], thereby limiting grain growth and generating a smaller surface area. The SEM microstructure depicted in Fig. 6a is clearly discernible a refined grain microstructure across the fusion zone for the welded sample P4. Figure 6b shows an enlarged SEM photograph of the yellow square marked in Fig. 6a. It provides a clear and comprehensive description of the characteristics of FZ and reveals a refined grain morphology with uniform dispersion of intermetallic phases. An intense pulse currents and frequencies resulted in controlled thermal cycles across the FZ and the dendritic structure of the welded sample were disintegrated, resulting in a refined microstructure used during welding, which aligns with Senthil's conclusions [16]. Additionally, spot EDS analysis (Fig. 6c and d) conducted on the

white particles shows the existence of significant Cu, Zn, and Mg along with Al, which confirms the presence of intermetallic phases viz. MgZn<sub>2</sub> and Al<sub>2</sub>CuMg were formed within the FZ during the welding process. The presence of these intermetallic phases indicates that the filler metal (ER5356) was evenly distributed in the FZ because they have similar chemical properties to AA7075 and contain significant amounts of Mg. The grain boundary melting and segregation are also observed to be low in the FZ for the welded sample P4, as shown in Fig. 6b, which are responsible for the improved mechanical properties of the joint [16, 24].

Figure 7 presents the XRD analysis findings for all the welded samples, illustrating the observed changes in phases within the weld metal of the joint. Similar to the AA7075-T6, the FZ still contained of MgZn<sub>2</sub> and Al<sub>2</sub>CuMg phases along with aluminium (Al). No additional intermetallic precipitates were observed in the XRD plot, indicating their thermal stability of MgZn<sub>2</sub> and Al<sub>2</sub>CuMg phases. As depicted in



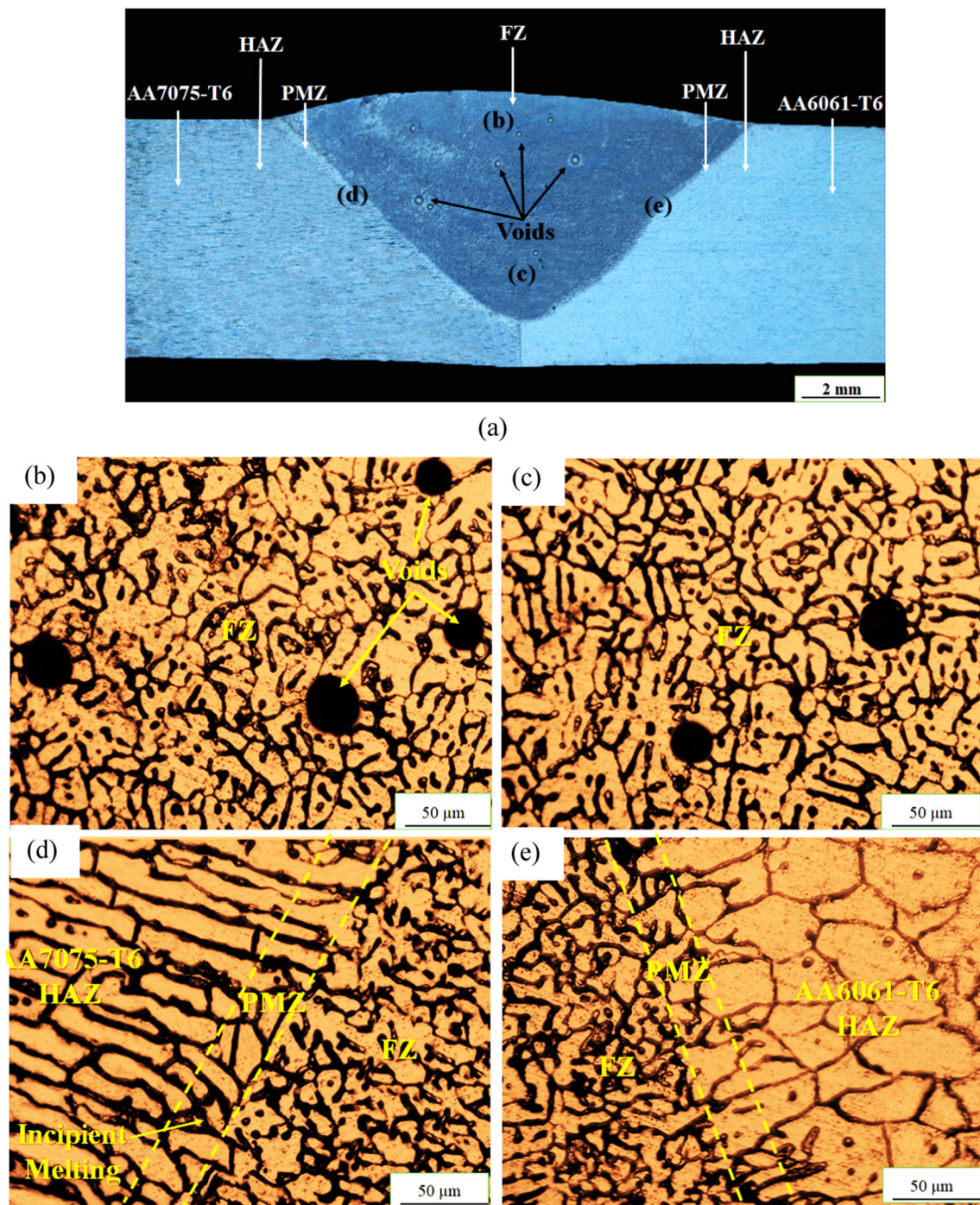


**Fig. 4** a Macrograph of the dissimilar P-TIG welded sample P1 (110 A, 4 Hz), the optical images depicting microstructural changes across a weld's cross-section at **b** FZ (top), **c** FZ (bottom), **d** HAZ/FZ interface (AA7075-T6 side), and **e** FZ/HAZ interface (AA6061-T6 side)

Figs. 3d and 7, the phase composition differed between the AA7075-T6 alloy and FZs due to a significant decrease in peak intensity ratios between the  $MgZn_2$  phase and the Al phase. Significantly less  $Al_2CuMg$  was present in the FZ than in the base metal AA7075-T6. In addition, the peak intensity in FZ varies considerably with peak current and pulse

frequency due to grain size, texture, grain migration, and sub-grain boundary movement during welding [44]. Raising the peak current from 110 to 175 A and peak frequency from 4 to 16 Hz, resulting in a notable decrease in peak intensities in the FZ as depicted in Fig. 7. The presence of relatively lower peak intensities for increased peak current



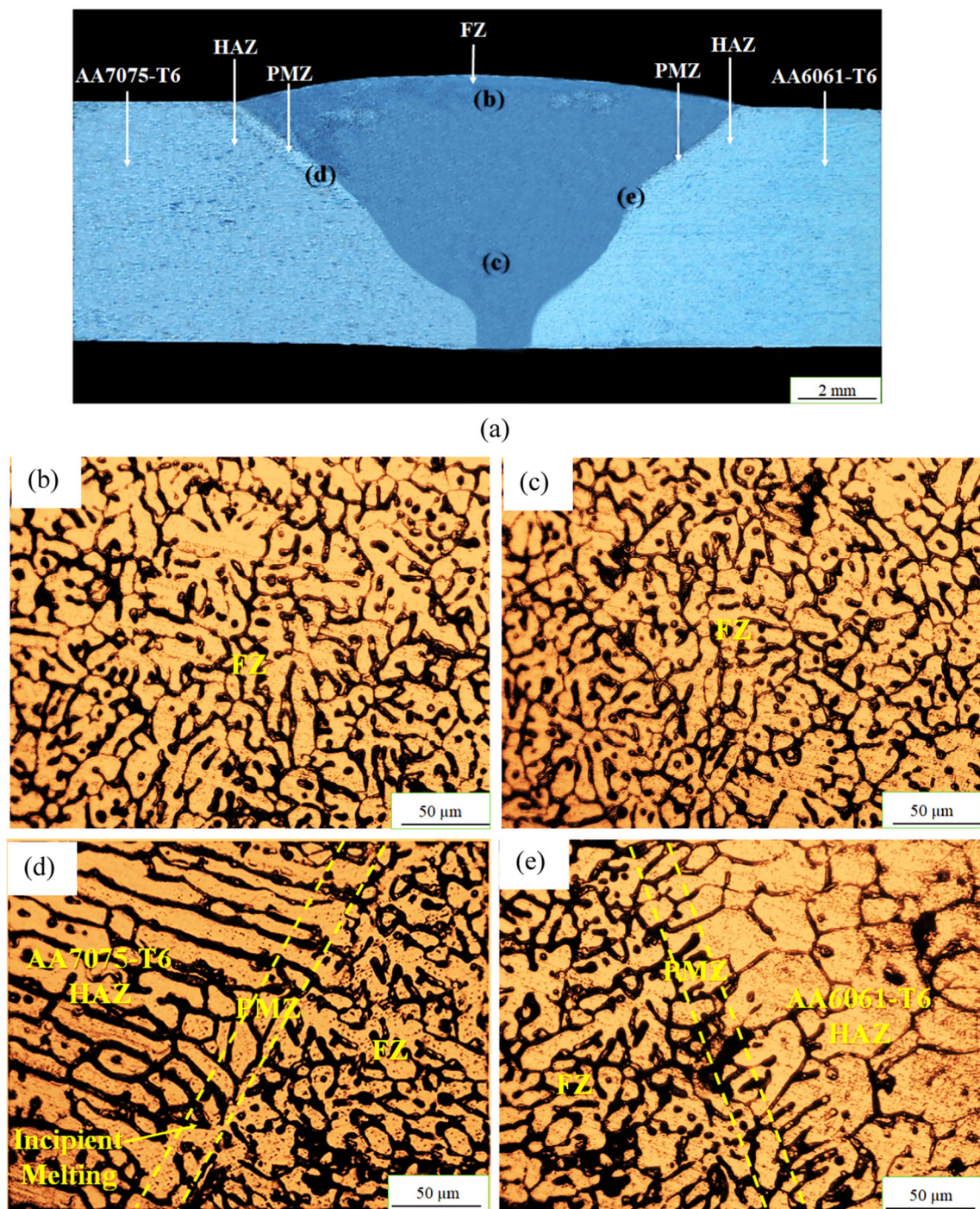


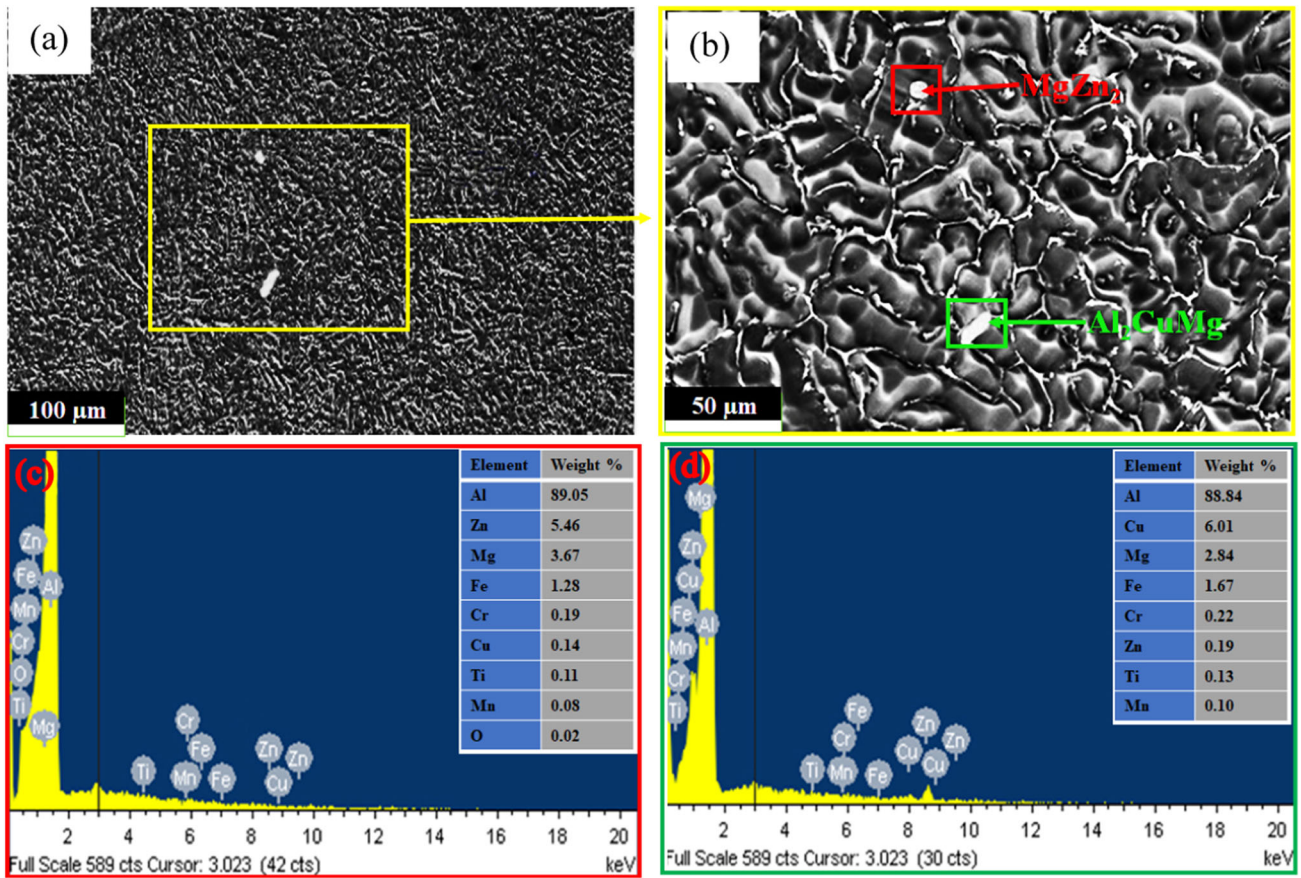
**Fig. 5** a Macrograph of the dissimilar P-TIG welded sample P1 (110 A, 4 Hz), the optical images depicting microstructural changes across a weld’s cross-section at **b** FZ (top), **c** FZ (bottom), **d** HAZ/FZ interface (AA7075-T6 side), and **e** FZ/HAZ interface (AA6061-T6 side)

and pulse frequency indicates that the intermetallic  $MgZn_2$  and  $Al_2CuMg$  precipitates were segregated at low levels, and most of them were fragmented resulting in improved mechanical properties [23].

Figure 8 represents the IPF (inverse pole figure) maps with colour-coded scale, grain size (GS) distribution, and

grain boundary MAs distribution across the FZ centre for P1 (110 A, 4 Hz) and P4 (175 A, 16 Hz) welded samples. The different colours in IPF maps represent crystallographic orientations of the various grains as displayed in Fig. 8a and d. An equiaxed and dendritic grains were observed across the FZ centre of P1 and P4 welded samples. According

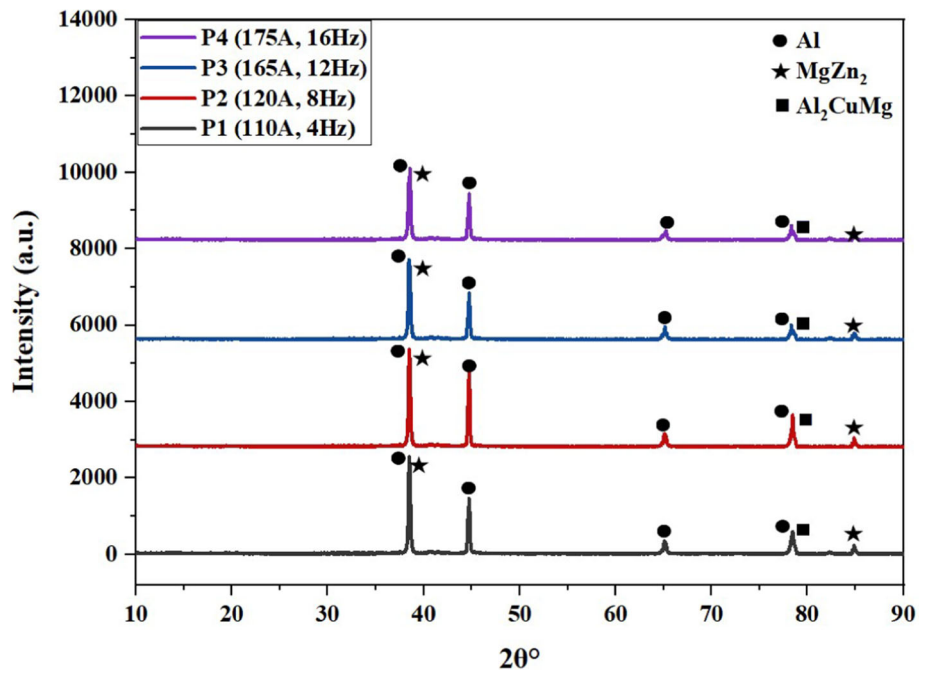




**Fig. 6** a SEM images showing microstructures of FZ for pulsed TIG welded sample P4 (175 A, 16 Hz); b magnified view of FZ showing different intermetallic phases; energy diffraction scanning results of

white particles in c red square region marked in b, and d green square region marked in b

**Fig. 7** XRD plots of P-TIG welded samples showing different peaks at different pulse currents and frequencies



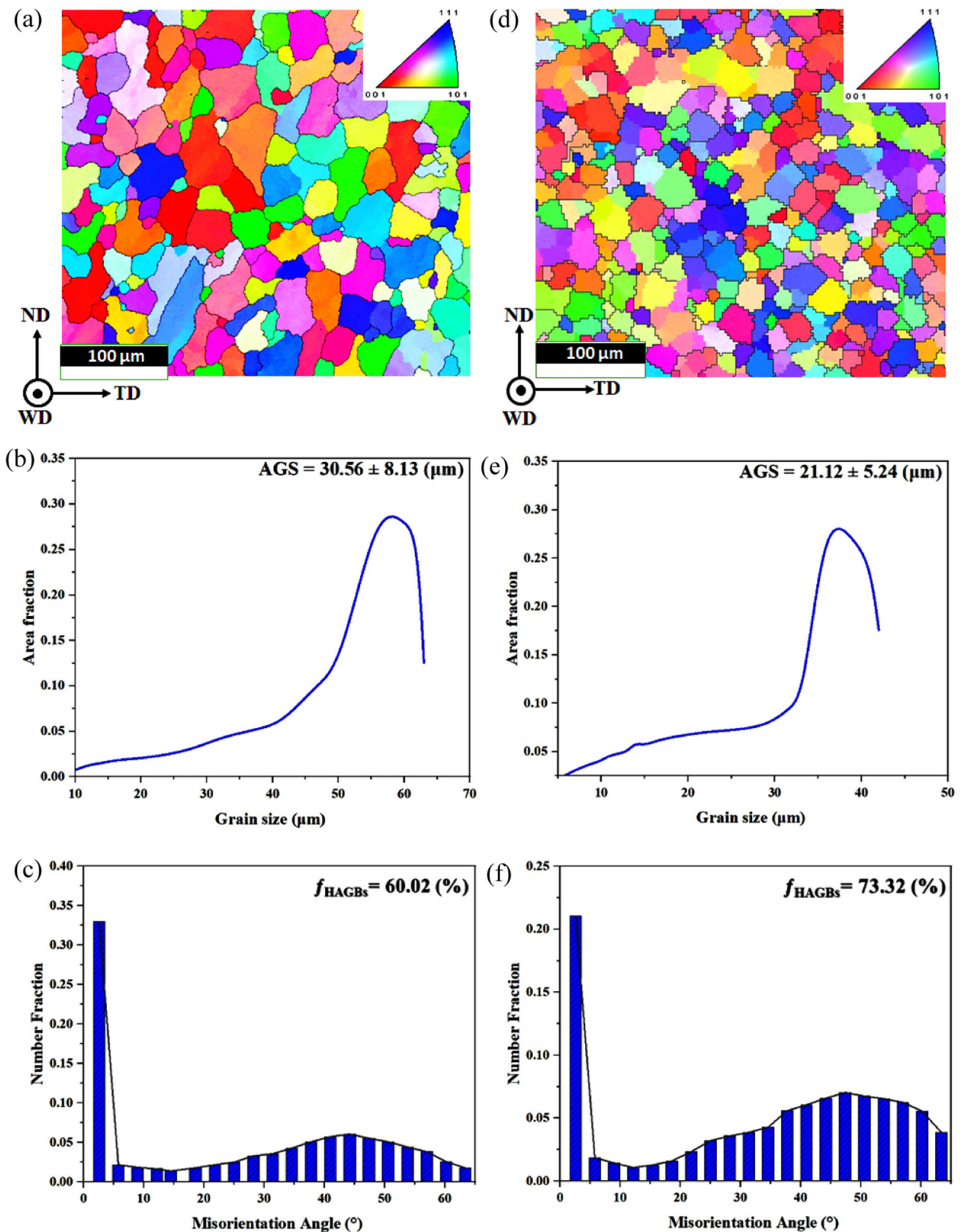


**Fig. 8** EBSD micrographs showing IPF map (including colour-coded scale), GS distribution and MAs distribution at the FZ centre of **a–c** P1 (110 A, 4 Hz) and **d–f** P4 (175 A, 16 Hz)



to the statistical results, the average grain size (AGS) for the welded sample P1 is  $30.56 \pm 8.13 \mu\text{m}$ , while AGS is  $21.12 \pm 5.24 \mu\text{m}$  for the welded sample P4 joint as shown in Fig. 8b and e. It can be addressed that the welded samples P4 at peak current 175 A with 16-Hz pulse frequency exhibited relatively fine grain structures compared to P1 welded sample having peak current 110 A with 4-Hz frequency. The pulse current frequency raised the frequency of the weld pool's continuous heating. This behaviour promoted dendritic remelting and detachment, leading to grain refining. The pulse current also boosted molten metal flow, enabling liquid metal to enter the pasting zone at elevated temperatures. Local heating in the pasting zone remelted and detached dendrites. Due of the electromigration effect, the pulsed electric current generated non-uniform Joule heat, leading to a significant current density at the tip of the dendrite. This raised temperature, allowing dendritic remelting and separation. Pulse current increased molten pool flow, transferring dendritic fragments to the whole pool and refining grain in the weld zone [6].

It was found in the literature that recrystallization is the main cause of the formation of new grains in the FZ during fusion welding of aluminium alloys [38, 45]. In the recrystallization process, the low-angle grain boundaries (LAGBs) of the base alloys keep moving and changing into high-angle grain boundaries (HAGBs) in the fusion region. This happens because sub-grains join together, making new recrystallized grains. The orientation maps (Fig. 8a and d) displayed colour-coded LAGBs with an average misorientation ranging from  $2^\circ$  to  $15^\circ$  and HAGBs with a misorientation exceeding  $15^\circ$ . For the welded sample P1, the proportion of HAGBs was 60.02%, while for the welded sample P4, the proportion of HAGBs was 73.32% as depicted in Fig. 8c and f. As the pulse current and pulse frequency are increased, the grain boundary transformations were more pronounced in the FZ. As the peak current and pulse frequency increased, a decrease in the AGS of the FZ, an increase in HAGBs, and a decrease in LAGBs were observed, indicating that the grain refinement and transformations are more favourable for the welded sample P4. The distribution of boundary MAs is primarily influenced by the heating and cooling cycles occurring during welding, specifically the maximum temperature achieved [45]. The weld sample P4 with a high peak current and pulse frequency causes a significant peak temperature increase in the FZ and a sharp temperature gradient across the grain boundaries. Enhanced diffusion at high peak temperatures can expedite the migration and metamorphosis of grain boundaries. This may result in a more significant transition from LAGBs to HAGBs. However, the welded sample P1 with no pulsing exhibited relatively coarser grains and lower HAGBs in the FZ, which may have detrimental consequences on the joint's mechanical characteristics. When a material is exposed to an external tensile force, dislocations tend to move more

slowly when there is a large concentration of HAGBs and fine grains. This causes dislocations to accumulate near the grain boundaries. Joint strength and ductility are improved as a consequence of the greater resistance to deformation under external tensile stress [46]. The transformations of LAGBs into HAGBs after welding have also been reported by many other researchers [46–48].

Texture strengthening occurs when a material's mechanical properties improve as a result of a significant change in its texture. Mechanical characteristics of welds are affected by their anisotropy, which may be assessed using texture analysis [46]. The texture formation is often associated with plastic deformation; however, achieving a well-defined texture in the cast structures of the welded joints can be challenging due to various factors, including the cooling rates and significant recrystallization associated with the fusion welding process [45]. In the present study, the degree of texture density variations in the base metals and welded joints (P1 and P4) across the centre of the FZ regions was analysed using the orientation distribution pole functions (ODFs). In Fig. 9a and b, the base metal AA6061-T6 had a maximum orientation density value of approximately 14.4, whereas the base metal AA7075-T6 had a maximum orientation density value of around 19.2. The welded sample P4 had only the highest orientation density value of approximately 6.7, while the welded sample P1 had a value of around 3.8, as depicted in Fig. 9c and d. The orientation density value of the welded joints was much lower than that of the base metals, suggesting that the texture was greatly reduced after welding [38, 49]. The variations in the texture orientation density value of the base metals and fusion zone resulted from distinct solidification behaviour. The base aluminium alloy was created through casting with a metal mould, and the molten material solidified in a specific direction to create the texture. The texture in the joints varies due to the different solidification processes in the weld molten pools and casting moulds. Reducing the texture can reduce the anisotropy of the mechanical properties [38].

### 3.3 Mechanical Properties

Table 5 provides a summary of the physical features of the P-TIG welded joints, such as ultimate tensile strength, percent elongation, joint efficiency, microhardness, and fracture position. The joint efficiency was calculated by dividing the ultimate tensile strength of the weld joint by the ultimate tensile strength of the base AA6061-T6 alloy [50]. Figure 10a depicts the engineering stress–strain curves for pulse TIG samples subjected to varying peak currents and pulse frequencies. The engineering stress–strain curves for base AA6061-T6 and AA7075-T6 alloys are also provided for the purpose of comparison. Base alloys are stronger and tougher than welded samples because of their fine casting

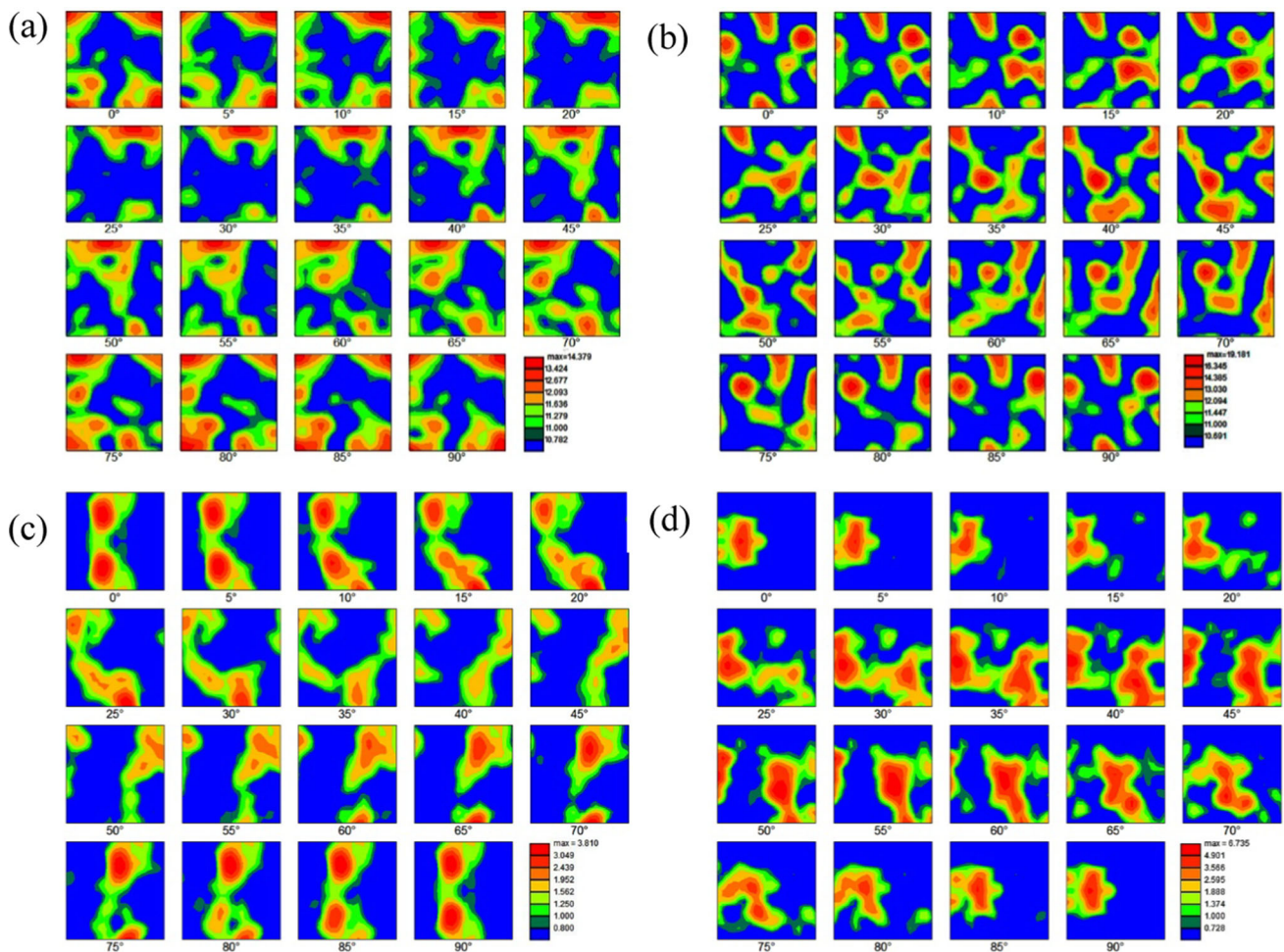


**Fig. 9** ODFs of the base metals and welded joints: **a** BM AA6061-T6, **b** BM AA7075-T6, **c** welded joint P1 (110 A, 4 Hz), and **d** welded joint P4 (175 A, 16 Hz)

**Table 5** The mechanical characteristics of the pulsed TIG welded joints

Sample	Peak current (A)	Pulse frequency (Hz)	Ultimate tensile strength (MPa)	Percent elongation (%)	Joint efficiency (%)	Vickers microhardness (HV)	Fracture position
P1	110	4	138 ± 1.25	5.2 ± 0.39	47.92 ± 0.67	79 ± 0.94	FZ
P2	120	8	146 ± 0.76	6.9 ± 2.24	50.69 ± 0.41	87 ± 2.10	FZ
P3	165	12	181 ± 1.95	10.6 ± 0.87	62.85 ± 1.04	95 ± 1.32	HAZ of AA6061-T6
P4	175	16	201 ± 2.17	16.8 ± 0.76	69.79 ± 1.16	101 ± 3.27	HAZ of AA6061-T6

structures and the presence of strengthening precipitates such as Mg<sub>2</sub>Si, MgZn<sub>2</sub>, and Al<sub>2</sub>CuMg [51].

The maximum ultimate tensile strength, percent elongation, and joint efficiency were approximately 201 MPa, 16.8%, and 69.79%, respectively, for welded sample P4, while welded sample P1 exhibited the ultimate tensile strength, percent elongation, and joint efficiency of 138 MPa,

5.9%, and 47.92%, respectively. The P1 joint had the lowest ultimate tensile strength, percent elongation, and joint efficiency compared to the other joints, which may be due to the shallower penetration of the weld and the development of voids in the FZ. Typically, the shield gas protects only the surface of the liquid metal puddle, while the back of the sample is not shielded. Consequently, air readily penetrates

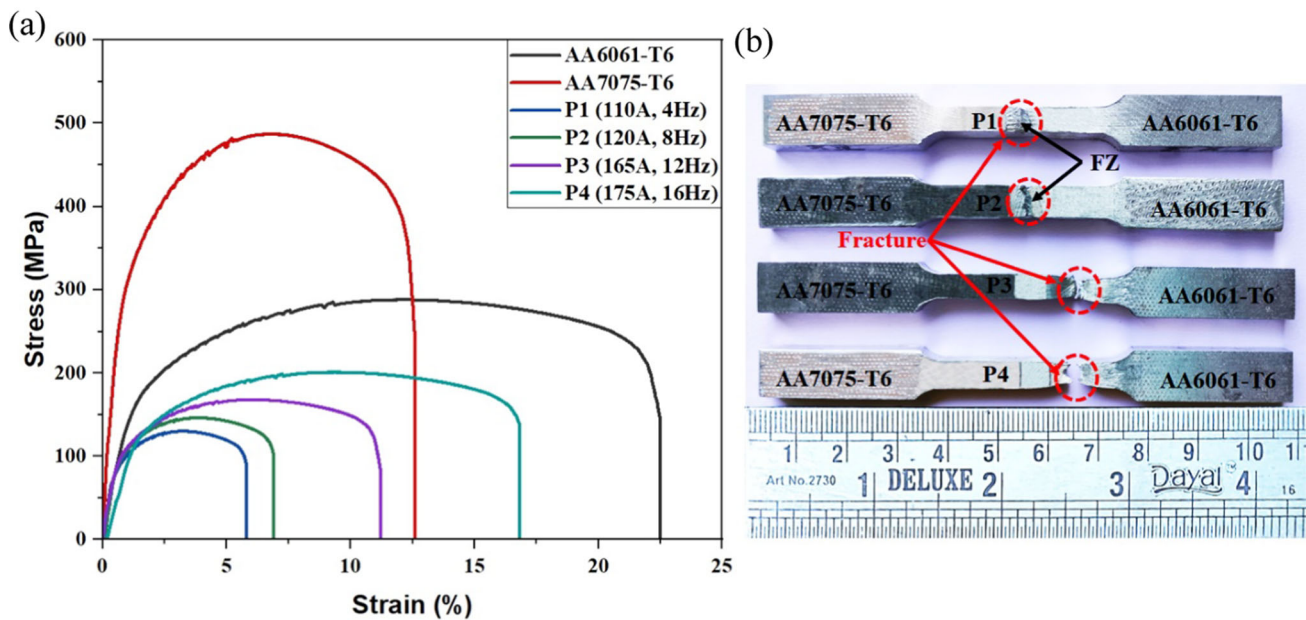


**Fig. 10** **a** Tensile stress–strain curves of the P-TIG welded samples and **b** the fractured position of the welded samples at various peak currents and pulse frequencies

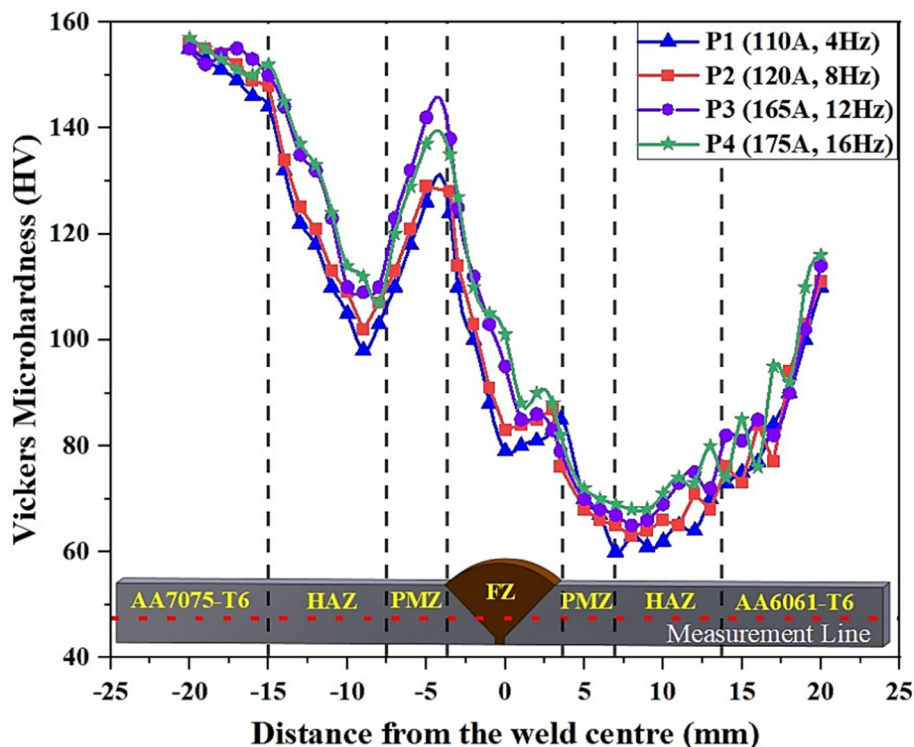
the liquid metal puddle, resulting in the formation of voids in the weld joints [52]. Lee [53] established a power–law relationship between AZ91 alloy tensile strength and vacancies. They found that voids considerably reduced both the ultimate tensile strength and percent elongation of the welded joints. The welded joint P4 exhibited the highest ultimate tensile strength and percent elongation compared with the other joints. Increased heat input resulted in relatively low cooling rates and prevented the molten pool from rapidly solidifying. Consequently, air has sufficient time to evacuate the molten pool, and the voids decrease. Additionally, in the welded joint P4, the secondary phases or precipitate-like phases were disseminated more evenly in the FZ (see Fig. 6b). Also, the AGS in the FZ ( $21.12 \pm 5.24 \mu\text{m}$ ) of the welded joint P4 is smaller than that in the FZ ( $30.56 \pm 8.13 \mu\text{m}$ ) of P1 (see Fig. 8b and e). Pulsed current welding enhances the weld’s strength by refining the grains and facilitating the uniform distribution of the intermetallic phases, which are effectively governed by the Mg, Zn, and Cu that accumulate in the weld matrix. In addition, the grain refinement and distribution of intermetallics in the fusion region were relatively lower for the welded sample P3 than for the welded sample P4. Thus, the effect of these elements on the solid solution precipitate hardening of the welded sample P3 was less than that of the welded sample P4. Based on the aforementioned discussions, it is possible to conclude that the welded sample P4 is stronger than the welded sample P3. Figure 10b demonstrates that weld samples P1 and P2 fractured at the FZ, whereas samples P3 and P4 fractured at

the HAZ of AA6061-T6, rather than at the FZ. This demonstrated that the welded samples P3 and P4 were stronger in the FZ than the welded samples P1 and P2, and that P4 was the strongest of the three.

Figure 11 shows the Vickers microhardness profile across the weld cross-section at various locations on the pulse TIG joints, which was approximately “W”-shaped profile [54]. The profile is asymmetrical compared to the FZ axial centre, suggesting different mechanical features of the joint on each side of this region. Due to the presence of strengthening elements, the base alloys exhibited high microhardness values, and the thermally affected zone (HAZ) exhibited a decreasing trend. Age hardening has caused an increase in hardness on both sides of PMZ just after the FZ (near the fusion boundary) as a consequence of a significant concentration of alloying elements in solid solution at the conclusion of the weld thermal cycle [50], while the decrease in hardness in HAZ is probably due to microstructural variations including grain coarsening and recrystallization, and the formation of coarse precipitates during welding [42]. Moreover, the microhardness drop was more severe from weld FZ to HAZ of AA7075-T6 aluminium alloy side. Since AA7075-T6 has lower thermal conductivity, less heat is transferred from this side to AA6061-T6 side, so weld heat is applied to this side for longer periods of time [43]. Accordingly, AA7075-T6 was more affected by weld heat than AA6061-T6 resulting more hardness drop in this side. As peak current and pulse frequency increased, the microhardness profile shifted upward, indicating a higher value. Tensile strength, as noted, is a significant material characteristic influenced by the porosities



**Fig. 11** Vickers microhardness distribution across the mid-thickness of P-TIG welded samples at various positions



within the FZ. Conversely, hardness is a localized attribute primarily determined by microstructural elements such as grain boundaries and grain size [55]. In actual, microhardness is also depending upon several other factors including temperature distribution, strain rate, elemental compositions, and intermetallic precipitates proportion appear to have an influence on the microhardness of the weld metal [56]. In accordance with the Hall–Petch correlation, the hardness strength shows an inverse correlation with grain size [57]. The welded sample P4 with the AGS in FZ (~ 21 μm) has the greatest hardness, while the welded sample P1 with AGS in FZ (~ 31 μm) has the lowest hardness. In addition, the transformation of LAGBs into HAGBs was greatest in the welded sample P4 joint (see Fig. 8f), which provides high resistance to local deformation during microhardness measurements.

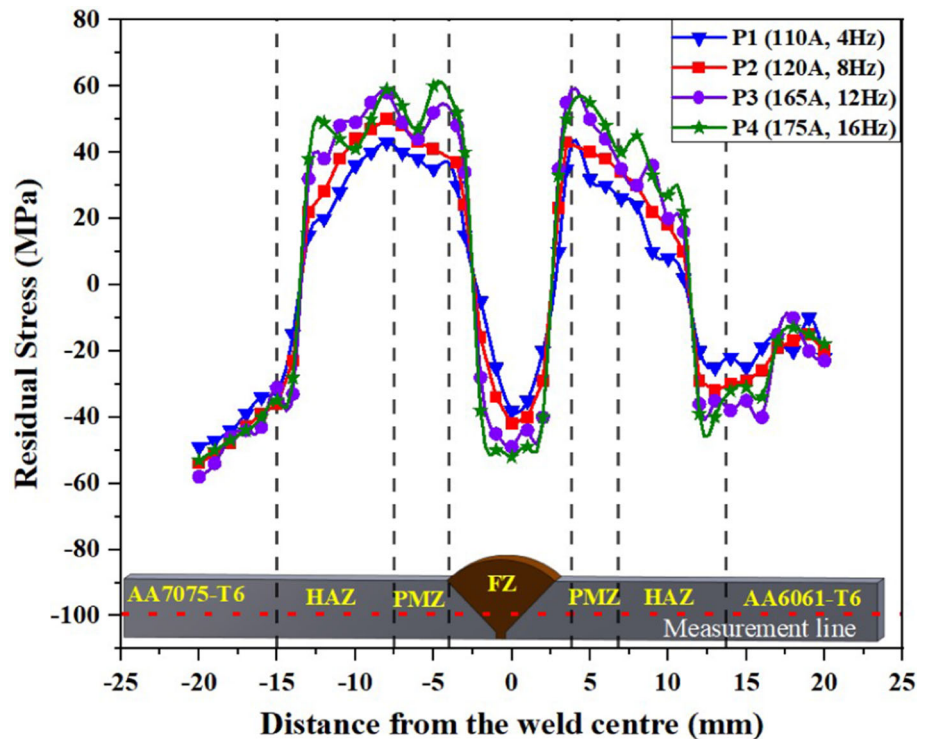
### 3.4 Residual Stress Characteristics

Residual stress pertains to the internal stresses retained within a material post-production and processing, without the influence of external forces or temperature variations [58]. The mechanical properties of pulsed TIG welded joints of AA6061-T6 and AA7075-T6 are profoundly influenced by residual stress and welding defects. During the TIG welding, intense localized heating and subsequent rapid cooling introduce residual stresses into the welded joints. These residual stresses, arising from uneven temperature gradients during

solidification, can lead to distortion and adversely impact the mechanical integrity of the joints [59]. In the case of aluminium alloys, such as AA6061-T6 and AA7075-T6, which are particularly sensitive to stress corrosion, residual stresses become a critical consideration as they may contribute to premature failure. Additionally, welding defects, including porosity, incomplete penetration, and solidification cracks, further affect the mechanical properties of the joints. Porosity, caused by gas entrapment during the welding process, creates voids that reduce the overall strength and ductility of the joint. Incomplete penetration limits the cross-sectional area of the weld, compromising joint strength. Solidification cracks, formed during the cooling phase, propagate through the material, diminishing the structural integrity of the joint. The alloy-specific characteristics of AA6061-T6 and AA7075-T6 also play a role, with AA7075-T6 being more prone to heat-affected zone (HAZ) softening during welding, potentially influencing joint strength.

The effect of high peak current in pulsed TIG welding on the joint performance of AA6061-T6 and AA7075-T6 is a critical aspect of welding parameters. High peak current (175 A) intensifies the heat input during welding, leading to rapid melting and solidification of the base metals. While this can enhance fusion and potentially increase joint strength (201 MPa), it also introduces challenges such as increased residual stresses. The elevated temperature gradients and cooling rates associated with high peak currents contribute to substantial residual stresses in the weld region.

**Fig. 12** Residual stress distributions across the mid-thickness of P-TIG welded samples at various positions



These stresses, if not properly managed, can adversely affect the tensile strength of the welded joint. Excessive residual stresses may lead to distortion, cracking, and reduced overall tensile strength [60]. The aluminium alloys AA6061-T6 and AA7075-T6 are particularly sensitive to the thermal effects of welding, and the interaction between high peak current and their metallurgical properties requires careful consideration.

Figure 12 shows the transverse residual stress profile at various locations along the mid cross-section of the welded samples, which resembles a “M” shape profile [50]. Different peak currents and pulse frequency clearly affect the residual stresses. Sample P4 (with a peak current of 175 A and a pulse frequency of 16 Hz) shows the highest magnitude of residual stress of 52 MPa, while sample P1 (with a peak current of 110 A and a pulse frequency of 4 Hz) shows the lowest magnitude of 38 MPa. Higher heat input concentration during welding led to increased differential heating and cooling cycles. Thus, the weld metal zones may experience increased strain due to thermal mismatch resulting from material and volume changes caused by different phase transitions. Residual stress increases when adjacent materials effectively constrain the heightened strains through either metallic continuity or base alloys clamping system restrictions [35]. Heterogeneous thermal strains from temperature fluctuations during welding and volume changes from phase transformations both have a role in determining the distribution of residual stress in welds [61]. The FZ had the highest residual stresses compared to

the thermally affected zone and base alloys in all the weldments. However, the surrounding regions help to counteract these stresses. Due to the higher elastic limit and better resistance to constraint, AA7075-T6 has slightly higher residual stress compared to AA6061-T6 in TIG welded joints. One can observe that the extent of residual stresses typically correlates with both the degree of constriction and the elastic limit of the weld metal [35]. Figure 13 displays the three-dimensional Debye ring, distortion curve, and residual stress profile curve for the P-TIG welded samples P1 (110 A, 4 Hz) and P4 (175 A, 16 Hz). Distortion rings show the location and full-width half maximum of the diffraction peak, while Debye rings have consistent radii at all angles. Greater distortion will occur due to inconsistencies in the diffraction angle if the material contains residual tension [62]. The residual stress profile at the weld bead indicates multiple peaks in the weld metal. Greater residual stresses are portrayed as redder peaks, whereas smaller residual stresses are shown in blue [58]. As shown in Fig. 13a, the distortions and red colour shade peaks in the profile curve of the welded sample P1 were small, suggesting that the residual stresses were also modest. However, as shown in Fig. 13b, the welded sample P4 exhibited the most severe distortions and the highest profile peak, suggesting the greatest residual stresses. These findings agree with those of other studies [35, 37, 58].

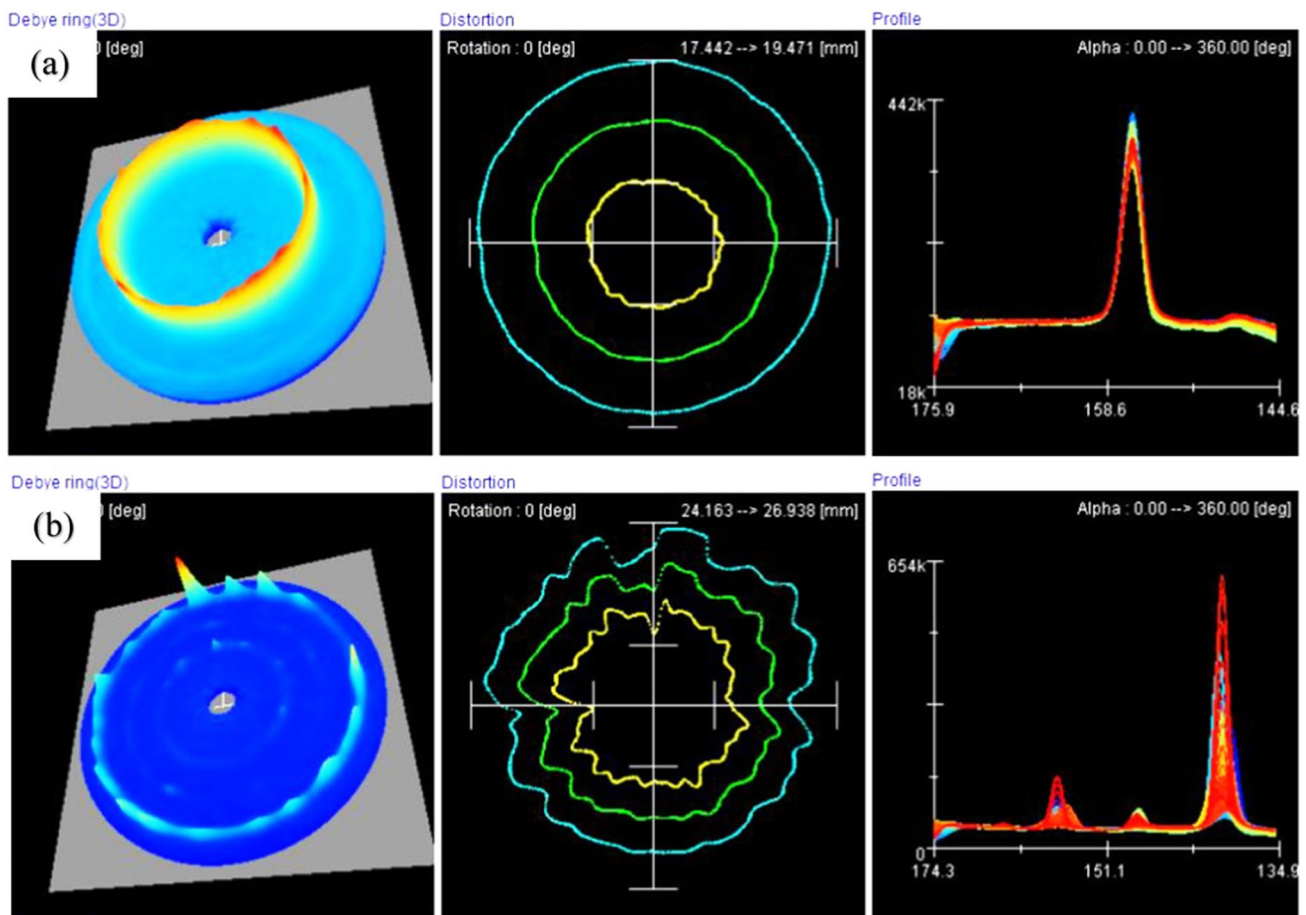


**Fig. 13** Three-dimensional Debye ring, distortion curves, and residual stress profile at the FZ centre of P-TIG welded samples **a** P1 (110 A, 4 Hz) and **b** P4 (175 A, 16 Hz)

### 3.5 Fractography

Figure 14a–d depicts SEM micrographs of the tensile fractured surfaces of the joints P1, P2, P3, and P4. Energy diffraction scanning analysis was also carried out to support the findings obtained from SEM analysis. Finer dimples result in increased joint strength and ductility, whereas coarser dimples have the opposite effect [52]. The fracture surface of the welded samples P1 and P2 (Fig. 14a and b) was characterized by a large rough cleavage facet with some macro-voids. These voids act as a stress concentrators and crack initiation sites, resulted brittle fracture mode [35]. The fractured surface of the welded samples P3 and P4 (Fig. 14c and d) displayed uniform and fine equiaxed dimples devoid of porosities, indicating ductile fracture mode. This clarified that the welded samples P3 and P4 elongated more than the other welded samples. The fracture surface of welded sample P4 exhibited uniform and fine dimples, leading to ductile fracture mode. EDS examination of the void region marked as green square region, revealed the presence of 0.92% Mg, 0.11% Ti, 4.53% O, 2.67% Cu, 1.42% Zn, 0.19% Cr, and

0.68% Fe along with aluminium (Fig. 14e). The fast-cooling rate associated with the welded sample P1 is responsible for the creation of voids in the FZ. During TIG welding, oxygen can get trapped in the molten pool attributed to its fast-cooling rate leading to the formation of these voids. This oxygen developed oxygen inclusion defects in the welded joint and could degrade the overall integrity of the weld joint and responsible for the brittle fracture in the FZ [35]. In addition to aluminium (Fig. 14f), the EDS examination of the highlighted yellow square area reveals the presence of 2.04% Mg, 3.21% Si, 0.72% Cu, 0.63% Zn, 0.20% Cr, and 1.91% Fe. Formation of intermetallic precipitates such as  $Mg_2Si$  at the fracture surfaces of the HAZ of the AA6061-T6 side is confirmed by the existence of a considerable quantity of Mg and Si. During welding, these intermetallic precipitates provide sufficient strength to the joint due to precipitation hardening. Therefore, during tensile test, the welded sample P4 showed significant necking before failure and responsible for the ductile fracture mode.



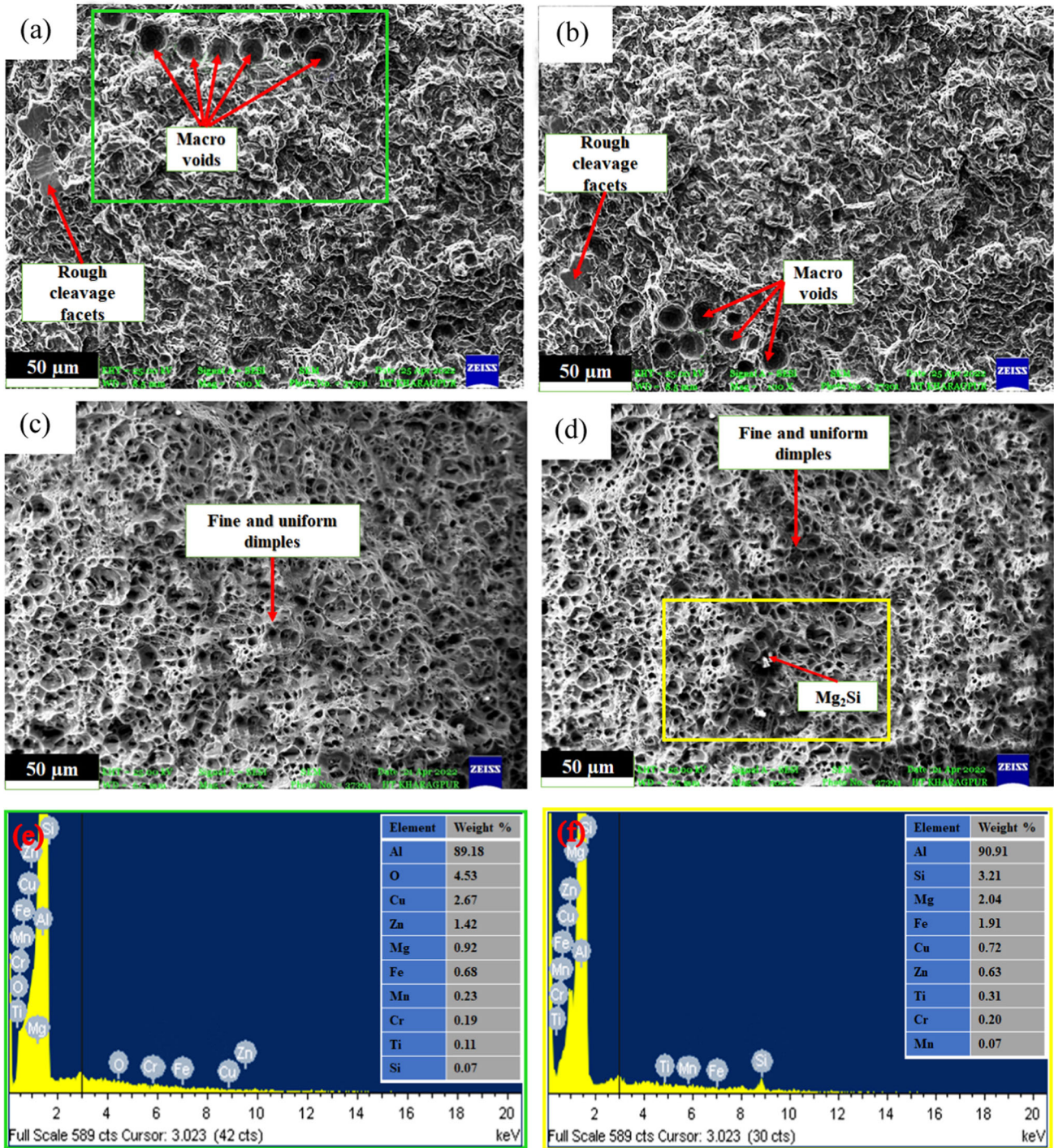


**Fig. 14** SEM images of tensile fractured surfaces of the pulse TIG joints **a** P1, **b** P2, **c** P3, and **d** P4; energy diffraction scanning results of marked square regions of fractured surfaces of the welded samples **e** P1 and **f** P4

## 4 Conclusions

The present investigation involved the successful fabrication of butt joints between 6-mm-thick dissimilar AA6061-T6 and AA7075-T6 aluminium plates using an automated P-TIG welding process. The effects of peak currents and pulse frequencies on microstructure, mechanical and residual stress characteristics of the dissimilar joint were examined. The findings from the experiment led to the following main conclusions:

1. Microstructural analysis showed that increasing the peak currents and pulse frequencies decreased the number of voids in the FZ, and SEM–EDS mapping showed that high peak currents and pulse frequencies led to less segregation of alloying elements.
2. EBSD analysis revealed that the welded sample P1 (110 A, 4 Hz) exhibited a coarse dendritic grain, with a high-angle grain boundaries (HAGBs) fraction of 60.02%, while the welded sample P4 (175 A, 16 Hz) exhibited a fine equiaxed grains, with large HAGBs fractions of 73.32%. Also, the maximum orientation density value of the welded joints was much lower than that of the base metals, suggesting that the texture was greatly reduced after welding.
3. The welded sample P4 developed a defect-free weld with the highest tensile strength (~ 201 MPa), percent elongation (~ 17%), microhardness (~ 101 HV), and compressive residual stresses (~ 76 MPa) compared to other welded samples. The welded sample P4 with high current pulsing resulted in improved mechanical and compressive residual stress properties due to ultrafine grains, lower segregation of alloying elements, and significant grain boundary strengthening.
4. The tensile fractured surface of the welded sample P1 (110 A, 4 Hz) exhibited coarse dimples with significant voids, resulting in a brittle fracture behaviour. However, the welded sample P4 (175 A, 16 Hz) exhibited a fractured surface with fine equiaxed dimples and no voids, resulting in ductile fracture behaviour.

Better quality joints and more productivity might be attained with the help of this research, which would also serve as a technical database for the aerospace and automobile sectors.

**Acknowledgements** The authors would like to thank the OIM & Texture Lab, Indian Institute of Technology, Bombay, for facilitating the EBSD characterization and the Precision Manufacturing Lab, Delhi Technological University, Delhi, for assisting with the residual stress characterization of the welded samples.

**Author's Contribution** MSBR worked in investigation, conceptualization, methodology, data curation, carried out the experiments, and

writing—original draft. ANS helped in reviewing and editing and supervision. HM contributed to reviewing and editing. QM helped in formal analysis and visualization.

**Funding** This research has not been supported by any financial resources.

## Declarations

**Conflict of Interest** On behalf of all authors, the corresponding author states that there is no conflict of interest.

## References

1. Nie, F.; Dong, H.; Chen, S.; Li, P.; Wang, L.; Zhao, Z., et al.: Microstructure and mechanical properties of pulse MIG welded 6061/A356 aluminum alloy dissimilar butt joints. *J. Mater. Sci. Technol.* **34**, 551–560 (2018). <https://doi.org/10.1016/j.jmst.2016.11.004>
2. Maissonnette, D.; Suery, M.; Nelias, D.; Chaudet, P.; Epicier, T.: Effects of heat treatments on the microstructure and mechanical properties of a 6061 aluminium alloy. *Mater. Sci. Eng. A* **528**, 2718–2724 (2011). <https://doi.org/10.1016/j.msea.2010.12.011>
3. Liu, C.; Northwood, D.O.; Bhole, S.D.: Tensile fracture behavior in CO<sub>2</sub> laser beam welds of 7075–T6 aluminum alloy. *Mater. Des.* **25**, 573–577 (2004). <https://doi.org/10.1016/j.matdes.2004.02.017>
4. Senthil Kumar, T.; Balasubramanian, V.; Babu, S.; Sanavullah, M.Y.: Effect of pulsed current GTA welding parameters on the fusion zone microstructure of AA 6061 aluminium alloy. *Met. Mater. Int.* **13**, 345–351 (2007)
5. Liu, J.; Zhu, H.; Li, Z.; Cui, W.; Shi, Y.: Effect of ultrasonic power on porosity, microstructure, mechanical properties of the aluminum alloy joint by ultrasonic assisted laser-MIG hybrid welding. *Opt. Laser Technol.* **119**, 105619 (2019). <https://doi.org/10.1016/j.optlastec.2019.105619>
6. Yuan, T.; Li, Y.; Ren, X.; Jiang, X.; Zhao, P.: Effect of pulse current on grain refinement in Ti6Al4V welds during pulsed plasma arc welding. *J. Mater. Eng. Perform.* (2023). <https://doi.org/10.1007/s11665-023-08543-8>
7. Janaki Ram, G.D.; Mitra, T.K.; Shankar, V.; Sundaresan, S.: Microstructural refinement through inoculation of type 7020 Al–Zn–Mg alloy welds and its effect on hot cracking and tensile properties. *J. Mater. Process. Technol.* **142**, 174–181 (2003). [https://doi.org/10.1016/S0924-0136\(03\)00574-0](https://doi.org/10.1016/S0924-0136(03)00574-0)
8. Babu, N.K.; Talari, M.K.; Pan, D.; Sun, Z.; Wei, J.; Sivaprasad, K.: Microstructural characterization and grain refinement of AA6082 gas tungsten arc welds by scandium modified fillers. *Mater. Chem. Phys.* **137**, 543–551 (2012). <https://doi.org/10.1016/j.matchemphys.2012.09.056>
9. Watanabe, T.; Shiroki, M.; Yanagisawa, A.; Sasaki, T.: Improvement of mechanical properties of ferritic stainless steel weld metal by ultrasonic vibration. *J. Mater. Process. Technol.* **210**, 1646–1651 (2010). <https://doi.org/10.1016/j.jmatprotec.2010.05.015>
10. Dong, H.; Yang, L.; Dong, C.; Kou, S.: Improving arc joining of Al to steel and Al to stainless steel. *Mater. Sci. Eng. A* **534**, 424–435 (2012). <https://doi.org/10.1016/j.msea.2011.11.090>
11. Zhang, L.; Jiang, H.; He, J.; Zhao, J.: Kinetic behaviour of TiB<sub>2</sub> particles in Al melt and their effect on grain refinement of aluminium alloys. *Trans. Nonferrous Met. Soc. China* **30**, 2035–2044 (2020). [https://doi.org/10.1016/S1003-6326\(20\)65358-4](https://doi.org/10.1016/S1003-6326(20)65358-4)
12. Xi, L.; Gu, D.; Guo, S.; Wang, R.; Ding, K.; Prashanth, K.G.: Grain refinement in laser manufactured Al-based composites with TiB<sub>2</sub>





- ceramic. *J. Mater. Res. Technol.* **9**, 2611–2622 (2020). <https://doi.org/10.1016/j.jmrt.2020.04.059>
13. Gu, J.; Ding, J.; Williams, S.W.; Gu, H.; Bai, J.; Zhai, Y., et al.: The strengthening effect of inter-layer cold working and post-deposition heat treatment on the additively manufactured Al–6.3Cu alloy. *Mater. Sci. Eng. A* **651**, 18–26 (2016). <https://doi.org/10.1016/j.msea.2015.10.101>
  14. Yuan, T.; Luo, Z.; Kou, S.: Grain refining of magnesium welds by arc oscillation. *Acta Mater.* **116**, 166–176 (2016). <https://doi.org/10.1016/j.actamat.2016.06.036>
  15. Yuan, T.; Kou, S.; Luo, Z.: Grain refining by ultrasonic stirring of the weld pool. *Acta Mater.* **106**, 144–154 (2016). <https://doi.org/10.1016/j.actamat.2016.01.016>
  16. Senthil Kumar, T.; Balasubramanian, V.; Sanavullah, M.Y.: Influences of pulsed current tungsten inert gas welding parameters on the tensile properties of AA 6061 aluminium alloy. *Mater. Des.* **28**, 2080–2092 (2007). <https://doi.org/10.1016/j.matdes.2006.05.027>
  17. Chen, K.; Zhan, L.; Xu, Y.; Liu, Y.: Effect of pulsed current density on creep-aging behavior and microstructure of AA7150 aluminum alloy. *J. Mater. Res. Technol.* **9**, 15433–15441 (2020). <https://doi.org/10.1016/j.jmrt.2020.10.100>
  18. Liu, J.; Staron, P.; Riekehr, S.; Stark, A.; Schell, N.; Huber, N., et al.: In situ study of phase transformations during laser-beam welding of a TiAl alloy for grain refinement and mechanical property optimization. *Intermetallics (Barking)* **62**, 27–35 (2015). <https://doi.org/10.1016/j.intermet.2015.03.003>
  19. Benakis, M.; Costanzo, D.; Patran, A.: Current mode effects on weld bead geometry and heat affected zone in pulsed wire arc additive manufacturing of Ti–6–4 and Inconel 718. *J. Manuf. Process.* **60**, 61–74 (2020). <https://doi.org/10.1016/j.jmapro.2020.10.018>
  20. Kumar, A.; Sundarajan, S.: Effect of welding parameters on mechanical properties and optimization of pulsed TIG welding of Al–Mg–Si alloy. *Int. J. Adv. Manuf. Technol.* **42**, 118–125 (2009). <https://doi.org/10.1007/s00170-008-1572-8>
  21. Kishore Babu, N.; Ganesh Sundara Raman, S.; Mythili, R.; Saroja, S.: Correlation of microstructure with mechanical properties of TIG weldments of Ti–6Al–4V made with and without current pulsing. *Mater Charact* **58**, 581–587 (2007). <https://doi.org/10.1016/j.matchar.2006.07.001>
  22. Yang, M.; Zheng, H.; Qi, B.; Yang, Z.: Effect of arc behavior on Ti–6Al–4V welds during high frequency pulsed arc welding. *J. Mater. Process. Technol.* **243**, 9–15 (2017). <https://doi.org/10.1016/j.jmatprotec.2016.12.003>
  23. Yelamasetti, B.; Rajyalakshmi, G.: Residual stress analysis, mechanical and metallurgical properties of dissimilar weldments of Monel 400 and AISI 316. *Int. J. Mater. Res.* **111**, 880–893 (2020). <https://doi.org/10.3139/146.111961>
  24. Dev, S.; Ramkumar, K.D.; Arivazhagan, N.; Rajendran, R.: Investigations on the microstructure and mechanical properties of dissimilar welds of inconel 718 and sulphur rich martensitic stainless steel, AISI 416. *J. Manuf. Process.* **32**, 685–698 (2018). <https://doi.org/10.1016/j.jmapro.2018.03.035>
  25. Devendranath Ramkumar, K.; Joshi, V.; Pandit, S.; Agrawal, M.; Kumar, O.S.; Periwal, S., et al.: Investigations on the microstructure and mechanical properties of multi-pass pulsed current gas tungsten arc weldments of Monel 400 and Hastelloy C276. *Mater. Des.* **64**, 775–782 (2014). <https://doi.org/10.1016/j.matdes.2014.08.055>
  26. Reddy, G.M.; Gokhale, A.A.; Rao, K.P.: Optimisation of pulse frequency in pulsed current gas tungsten arc welding of aluminium–lithium alloy sheets. *Mater. Sci. Technol.* **14**, 61–66 (1998). <https://doi.org/10.1179/mst.1998.14.1.61>
  27. Yelamasetti, B.; Ramana, G.V.; Manikyam, S.; Vardhan, T.V.: Thermal field and residual stress analyses of similar and dissimilar weldments joined by constant and pulsed current TIG welding techniques. *Adv. Mater. Process. Technol.* **8**, 1889–1904 (2022). <https://doi.org/10.1080/2374068X.2021.1959114>
  28. Ishak, M.; MohdNoordin, N.F.; Ahmad Shah, L.H.: Feasibility study on joining dissimilar aluminum alloys AA6061 and AA7075 by tungsten inert gas (TIG). *J. Teknol* (2015). <https://doi.org/10.1113/jt.v75.5177>
  29. Mehdi, H.; Mishra, R.S.: Microstructure and mechanical characterization of tungsten inert gas-welded joint of AA6061 and AA7075 by friction stir processing. *Proc. Inst. Mech. Eng. Part L J. Mater. Design Appl.* **235**, 2531–2546 (2021). <https://doi.org/10.1177/14644207211007882>
  30. Yamada, R.; Ishizawa, S.; Itoh, G.; Kurumada, A.; Nakai, M.: Effects of environment on fatigue crack growth behavior of 2000 and 7000 series aluminum alloys. In: *Recent Advances in Structural Integrity Analysis—Proceedings of the International Congress (APCF/SIF-2014)*, pp. 123–6. Elsevier (2014). <https://doi.org/10.1533/9780081002254.123>
  31. Madadi, F.; Ashrafizadeh, F.; Shamanian, M.: Optimization of pulsed TIG cladding process of stellite alloy on carbon steel using RSM. *J. Alloys Compd.* **510**, 71–77 (2012). <https://doi.org/10.1016/j.jallcom.2011.08.073>
  32. Balram, Y.; Vishu Vardhan, T.; Sridhar Babu, B.; Venkat Ramana, G.; Preethi, Ch.: Thermal stress analysis of AISI 316 stainless steels weldments in TIG and pulse TIG welding processes. *Mater. Today Proc.* **19**, 182–187 (2019). <https://doi.org/10.1016/j.matpr.2019.06.695>
  33. Giridharan, P.K.; Murugan, N.: Optimization of pulsed GTA welding process parameters for the welding of AISI 304L stainless steel sheets. *Int. J. Adv. Manuf. Technol.* **40**, 478–489 (2009). <https://doi.org/10.1007/s00170-008-1373-0>
  34. Lin, J.; Ma, N.; Lei, Y.; Murakawa, H.: Measurement of residual stress in arc welded lap joints by  $\cos\alpha$  X-ray diffraction method. *J. Mater. Process. Technol.* **243**, 387–394 (2017). <https://doi.org/10.1016/j.jmatprotec.2016.12.021>
  35. Bin Reyaz, M.S.; Sinha, A.N.: Analysis of mechanical properties and optimization of tungsten inert gas welding parameters on dissimilar AA6061-T6 and AA7075-T6 by a response surface methodology-based desirability function approach. *Eng. Optim.* (2023). <https://doi.org/10.1080/0305215X.2023.2230133>
  36. Chen, C.; Sun, G.; Du, W.; Li, Y.; Fan, C.; Zhang, H.: Influence of heat input on the appearance, microstructure and microhardness of pulsed gas metal arc welded Al alloy weldment. *J. Mater. Res. Technol.* **21**, 121–130 (2022). <https://doi.org/10.1016/j.jmrt.2022.09.028>
  37. Koli Y.; Yuvaraj N.; Aravindan S.; Vipin: CMT Joining of AA6061-T6 and AA6082-T6 and examining mechanical properties and microstructural characterization. *Trans. Indian Inst. Met.* **74**, 313–29 (2021). <https://doi.org/10.1007/s12666-020-02134-0>
  38. Qin, Q.; Zhao, H.; Li, J.; Zhang, Y.; Zhang, B.; Su, X.: Microstructures and mechanical properties of TIG welded Al–Mg2Si alloy joints. *J. Manuf. Process.* **56**, 941–949 (2020). <https://doi.org/10.1016/j.jmapro.2020.05.058>
  39. Moradi, M.M.; Jamshidi Aval, H.; Jamaati, R.; Amir Khanlou, S.; Ji, S.: Microstructure and texture evolution of friction stir welded dissimilar aluminum alloys: AA2024 and AA6061. *J. Manuf. Process.* **32**, 1–10 (2018). <https://doi.org/10.1016/j.jmapro.2018.01.016>
  40. Song, G.; Wang, Z.; Liu, Z.; Liu, L.: Effect of partial rolling on the microstructure and mechanical properties of laser-TIG hybrid welded joints of 7075–T6 aluminum alloy. *Int. J. Adv. Manuf. Technol.* **121**, 589–599 (2022). <https://doi.org/10.1007/s00170-022-09287-w>
  41. Temmar, M.; Hadji, M.; Sahraoui, T.: Effect of post-weld aging treatment on mechanical properties of Tungsten Inert Gas welded low thickness 7075 aluminium alloy joints. *Mater. Des.* **32**, 3532–3536 (2011). <https://doi.org/10.1016/j.matdes.2011.02.011>
  42. Hakem, M.; Lebaili, S.; Mathieu, S.; Miroud, D.; Lebaili, A.; Cheniti, B.: Effect of microstructure and precipitation phenomena on the mechanical behavior of AA6061-T6 aluminum alloy weld. *Int. J.*





- Adv. Manuf. Technol. **102**, 2907–2918 (2019). <https://doi.org/10.1007/s00170-019-03401-1>
43. Çömez, N.; Durmus, H.: Cold metal transfer welding of AA6061 to AA7075: Mechanical properties and corrosion. *J. Eng. Mater. Technol. Trans. ASME* (2019). <https://doi.org/10.1115/1.4042863>
  44. Eftekhar, A.H.; Sadrossadat, S.M.; Reihanian, M.: Effect of heat input on microstructure and mechanical properties of TIG-welded semisolid cast AXE622 Mg alloy. *Mater Charact* (2022). <https://doi.org/10.1016/j.matchar.2021.111692>
  45. Li, S.; Dong, H.; Wang, X.; Liu, Z.; Tan, Z.; Shangguan, L., et al.: Effect of repair welding on microstructure and mechanical properties of 7N01 aluminum alloy MIG welded joint. *J. Manuf. Process.* **54**, 80–88 (2020). <https://doi.org/10.1016/j.jmapro.2020.03.009>
  46. Verma, M.; Saha, P.: Effect of micro-grooves featured tool and their depths on dissimilar micro-friction stir welding ( $\mu$ FSW) of aluminum alloys: a study of process responses and weld characteristics. *Mater Charact* (2023). <https://doi.org/10.1016/j.matchar.2022.112614>
  47. Zhao, H.; Yu, M.; Jiang, Z.; Zhou, L.; Song, X.: Interfacial microstructure and mechanical properties of Al/Ti dissimilar joints fabricated via friction stir welding. *J. Alloys Compd.* **789**, 139–149 (2019). <https://doi.org/10.1016/j.jallcom.2019.03.043>
  48. Zhao, H.; Pan, Q.; Qin, Q.; Wu, Y.; Su, X.: Effect of the processing parameters of friction stir processing on the microstructure and mechanical properties of 6063 aluminum alloy. *Mater. Sci. Eng. A* **751**, 70–79 (2019). <https://doi.org/10.1016/j.msea.2019.02.064>
  49. Yan, S.; Ma, C.; Chen, H.: Modifying microstructures and mechanical properties of laser-arc welded joints of dissimilar advanced aluminum alloys. *Mater Charact* **164**, 110331 (2020). <https://doi.org/10.1016/j.matchar.2020.110331>
  50. Bin Reyaz, M.S.; Sinha, A.N.: An experimental investigation on mechanical characteristics and wear behaviour of TIG welded dissimilar aluminum alloys. *J. Adhes. Sci. Technol.* (2023). <https://doi.org/10.1080/01694243.2023.2251782>
  51. Bahemmat, P.; Haghpanahi, M.; Besharati, M.K.; Ahsanizadeh, S.; Rezaei, H.: Study on mechanical, micro-, and macrostructural characteristics of dissimilar friction stir welding of AA6061-T6 and AA7075-T6. *Proc. Inst. Mech. Eng. B J. Eng. Manuf.* **224**, 1854–1865 (2010). <https://doi.org/10.1243/09544054JEM1959>
  52. Peng, D.; Shen, J.; Tang, Q.; Wu, C.P.; Zhou, Y.B.: Effects of aging treatment and heat input on the microstructures and mechanical properties of TIG-welded 6061–T6 alloy joints. *Int. J. Miner. Metall. Mater.* **20**, 259–265 (2013). <https://doi.org/10.1007/s12613-013-0721-8>
  53. Do Lee, C.: Effect of grain size on the tensile properties of magnesium alloy. *Mater. Sci. Eng. A* **459**, 355–360 (2007). <https://doi.org/10.1016/j.msea.2007.01.008>
  54. Murali, N.; Li, X.: TIG Welding of Dissimilar High-Strength Aluminum Alloys 6061 and 7075 with Nano-Treated Filler Wires. *Minerals, Metals and Materials Series*, Vol. 6, p. 316–322. Springer Science and Business Media Deutschland GmbH, Berlin (2021) [https://doi.org/10.1007/978-3-030-65396-5\\_47](https://doi.org/10.1007/978-3-030-65396-5_47)
  55. Deore, H.A.; Mishra, J.; Rao, A.G.; Mehtani, H.; Hiwarkar, V.D.: Effect of filler material and post process ageing treatment on microstructure, mechanical properties and wear behaviour of friction stir processed AA 7075 surface composites. *Surf. Coat. Technol.* **374**, 52–64 (2019). <https://doi.org/10.1016/j.surfcoat.2019.05.048>
  56. Tariq, M.; Khan, I.; Hussain, G.; Farooq, U.: Microstructure and micro-hardness analysis of friction stir welded bi-layered laminated aluminum sheets. *Int. J. Lightweight Mater. Manuf.* **2**, 123–130 (2019). <https://doi.org/10.1016/j.ijlmm.2019.04.010>
  57. Alam, M.P.; Sinha, A.N.: Effect of heat assisting backing plate in friction stir welding of high strength Al-Li alloy. *Energy Sources Part A Recover. Util. Environ. Effects* **44**, 2851–2862 (2022). <https://doi.org/10.1080/15567036.2019.1651793>
  58. Roy, J.G.; Yuvaraj, N.; Vipin.: Effect of welding parameters on mechanical properties of cold metal transfer welded thin AISI 304 stainless-steel sheets. *Trans. Indian Inst. Met.* **74**, 2397–408 (2021). <https://doi.org/10.1007/s12666-021-02326-2>
  59. Mehdi, H.; Mishra, R.S.: Influence of friction stir processing on weld temperature distribution and mechanical properties of TIG-welded joint of AA6061 and AA7075. *Trans. Indian Inst. Met.* **73**, 1773–1788 (2020). <https://doi.org/10.1007/s12666-020-01994-w>
  60. Mehdi, H.; Mishra, R.S.: Effect of friction stir processing on mechanical properties and wear resistance of tungsten inert gas welded joint of dissimilar aluminum alloys. *J. Mater. Eng. Perform.* **30**, 1926–1937 (2021). <https://doi.org/10.1007/s11665-021-05549-y>
  61. Mehdi, B.; Badji, R.; Ji, V.; Allili, B.; Bradai, D.; Deschaux-Beaume, F., et al.: Microstructure and residual stresses in Ti-6Al-4V alloy pulsed and unpulsed TIG welds. *J. Mater. Process. Technol.* **231**, 441–448 (2016). <https://doi.org/10.1016/j.jmatprotec.2016.01.018>
  62. Bector, K.; Singh, M.; Pandey, D.; Butola, R.; Singari, R.M.: Study of residual stresses in multi-pass friction stir processed surface composites. *Adv. Mater. Process. Technol.* (2021). <https://doi.org/10.1080/2374068X.2021.1939983>

Springer Nature or its licensor (e.g. a society or other partner) holds exclusive rights to this article under a publishing agreement with the author(s) or other rightsholder(s); author self-archiving of the accepted manuscript version of this article is solely governed by the terms of such publishing agreement and applicable law.

